

Niobium quantum interference microwave circuits with monolithic three-dimensional nanobridge junctions

Kevin Uhl[✉],* Daniel Hackenbeck, Janis Peter[✉], Reinhold Kleiner[✉], Dieter Koelle[✉], and Daniel Bothner[✉]†

Physikalisches Institut, Center for Quantum Science (CQ) and LISA⁺, Universität Tübingen, Tübingen 72076, Germany

 (Received 26 May 2023; revised 10 November 2023; accepted 25 January 2024; published 27 February 2024)

Nonlinear microwave circuits are key elements for many groundbreaking research directions and technologies, such as quantum computation and quantum sensing. The majority of microwave circuits with Josephson nonlinearities to date are based on aluminum thin films; therefore, they are severely restricted in their operation range regarding temperatures and external magnetic fields. Here, we present the realization of superconducting niobium microwave resonators with integrated, three-dimensional (3D) nanobridge-based superconducting quantum interference devices. The 3D nanobridges (constriction weak links) are monolithically patterned into prefabricated microwave *LC* circuits using neon focused-ion-beam milling, and the resulting quantum interference circuits show frequency tunabilities, flux responsivities, and Kerr nonlinearities on par with comparable aluminum nanobridge devices, but with the perspective of a much larger operation parameter regime. Our results demonstrate that neon focused-ion-beam milling is a promising method for fabricating 3D constriction junctions with flexible parameters and reveal great potential for application of the resulting microwave circuits in hybrid systems with, e.g., magnons and spin ensembles or in flux-mediated optomechanics.

DOI: [10.1103/PhysRevApplied.21.024051](https://doi.org/10.1103/PhysRevApplied.21.024051)

I. INTRODUCTION

Superconducting microwave circuits with integrated Josephson junctions (JJs) and superconducting quantum interference devices (SQUIDs) have led to groundbreaking experimental and technological developments in recent decades. Both single JJs and SQUIDs constitute a flexible and designable Josephson or Kerr nonlinearity, while a SQUID additionally provides *in situ* tunability of the resonance frequency by external magnetic flux. Circuits with large nonlinearities originating from the Josephson element form artificial atoms and qubits [1,2], which have been used for spectacular experiments in circuit quantum electrodynamics [3] and quantum information processing [4]. Frequency-tunable devices with a small nonlinearity are highly relevant for quantum-limited Josephson parametric amplifiers [5–7], tunable microwave cavities for hybrid systems with spin ensembles and magnons, dispersive SQUID magnetometry [8,9], photon-pressure systems [10–13], and microwave optomechanics [14–17].

In many of these currently active research fields, such as flux-mediated optomechanics, hybrid quantum devices with magnonic oscillators and dispersive SQUID

magnetometry, it is highly desirable to have frequency-tunable microwave circuits with small nonlinearity, high magnetic field tolerance, and (in some cases) a critical temperature significantly above that of aluminum. The vast majority of frequency-tunable and nonlinear circuits, however, use Josephson junctions and SQUIDs made of aluminum thin films [18,19], a superconducting material with a critical magnetic field of only $B_c \sim 10\text{--}100$ mT and a critical temperature $T_c \approx 1.2\text{--}1.5$ K for convenient film thicknesses $\gtrsim 100$ nm [20]. For much thinner films or material variations such as granular aluminum, the critical fields and temperatures can be considerably higher [20–22], but at the expense of a very high kinetic inductance, a property often detrimental to high-performance SQUID operation. An approach that could fulfil the aforementioned wish list is the implementation of microwave circuits made of niobium [23], niobium alloys [24,25], or even a high- T_c superconductor such as YBCO [26–28] with high critical current density and high-field-compatible Josephson elements such as nanoconstrictions [29–31]. In most efforts so far, however, it has proven difficult to obtain large-tunability constriction-junction SQUIDs made of these materials, both in the direct-current (dc) operation mode and in the microwave domain [30,32–35].

Here, we report the realization of niobium superconducting quantum interference microwave circuits based on

*kevin.uhl@pit.uni-tuebingen.de

†daniel.bothner@uni-tuebingen.de

neon focused-ion-beam (Ne-FIB) patterned monolithic 3D nanobridge junctions. Although the SQUIDs in our devices have a large effective area of about $72 \mu\text{m}^2$, we achieve smaller screening parameters than previous 2D niobium nanobridge SQUID circuits with much smaller loops [30]. A small screening parameter is an important prerequisite for stable flux tunability of the circuit resonance frequency and large flux responsivities [36]. In addition, we characterize our nanobridge quantum interference circuits at varying temperatures in the regime $2.4 < T_s < 3.4$ K and demonstrate that they have a small Kerr nonlinearity of $|\mathcal{K}|/2\pi \lesssim 10$ kHz, ideal for large dynamic range applications. Our devices and results show great potential for dispersive SQUID magnetometry, hybrid systems with spin ensembles, magnons or cold atoms, and flux-mediated optomechanics.

II. DEVICES

Our devices are lumped-element microwave circuits, patterned from a $d_{\text{Nb}} = 90$ -nm-thick layer of dc magnetron sputtered niobium on top of a high-resistivity silicon substrate with thickness $d_{\text{Si}} = 500 \mu\text{m}$. The niobium film has a transition temperature $T_c \approx 8.6$ K and a zero-temperature penetration depth $\lambda_0 \approx 155$ nm (see Note II within the Supplemental Material [37]), and comparable films show residual normal-state resistivities of $\rho_{\text{Nb}} \sim 8\text{--}10 \mu\Omega \text{cm}$ at 10 K. The circuits consist of two interdigitated capacitors (IDCs) combined in parallel and several linear inductors, and they are capacitively side coupled to a $Z_0 \approx 50 \Omega$ coplanar waveguide transmission line by means of a coupling capacitance C_c for driving and readout. One of the devices and its circuit equivalent are shown in Figs. 1(a) and 1(b), respectively. The width of all lines (fingers and inductor wires) and the gaps in between two adjacent IDC fingers is $W = 3 \mu\text{m}$. At the connection point between the capacitors and the inductor wires, a square-shaped loop with an effective area of about $8.5 \times 8.5 \mu\text{m}^2$ (hole size $6 \times 6 \mu\text{m}^2$) is embedded into the circuit, which forms the SQUID once the nanoconstrictions are introduced; see Figs. 1(c) and 1(d).

After patterning the circuit itself by means of optical lithography and reactive ion etching using SF_6 , the nanoconstrictions are fabricated into the center of the two loop arms using a neon focused ion beam. For the simplest constrictions, we cut a narrow 20-nm-wide slot from both sides into each of the two loop arms, leaving only a 40-nm-wide constriction in the center of each arm. This type of constriction (thickness equal for the leads and the constriction) has been referred to as 2D constriction and has been implemented for both dc and microwave SQUIDs in the past [30,32,33]. It has also been demonstrated, however, that 3D versions, i.e., constrictions that are thinner than the superconducting leads connected to them, can have superior properties such as less skewed

current-phase relations, smaller critical currents, and lower flux noise [9,32,38,39]. Furthermore, implementing 3D constrictions, although usually very challenging to fabricate, allows one to keep the circuit film thickness large, i.e., the circuit and loop kinetic inductance small, while at the same time getting a critical junction current $I_0 \sim 10 \mu\text{A}$, a highly desirable range for simultaneously achieving a large frequency tunability and a small circuit nonlinearity.

For implementation of the 3D versions, we therefore modify our ion beam scan pattern in a way that the constriction is thinned down during the cutting procedure [see Fig. 1(e)]; more details can be found in Appendix A. Such a monolithic and so far unexplored Ne-FIB-based approach for the generation of 3D nanobridges circumvents some of the challenges and possible problems of previously implemented multilayer deposition processes, such as guaranteeing good galvanic contact between the layers or dealing with thin additional edges at the bottom of the microwave structures [38,39], two problems that get increasingly challenging with decreasing constriction thickness. Single-layer processes using electron-beam lithography (EBL) and reactive ion etching or lift-off on the other hand cannot be used for the fabrication of 3D bridges. Ne FIB furthermore allows one to retrim prepatterned nanoconstrictions with relative ease compared to EBL due to the limited multilayer alignment accuracy of typical EBL machines and the inevitable resist involved. FIB techniques can finally be used on very uneven samples, something hard to implement with classical lithography techniques. In principle, our fabrication method for 3D constrictions can also be implemented using other materials such as aluminum, lead, titanium, or niobium alloys, and it will be interesting to study the properties of such circuits nanopatterned by Ne FIB and to compare them with those obtained using established techniques.

In addition to the manufacturing advantages, our approach offers the unique opportunity to characterize one and the same microwave circuit both without and with the junctions, i.e., one can experimentally determine the impact of the junctions on the circuit properties. In reverse, we can also extract with high reliability the properties of the constrictions themselves, such as the critical currents as a function of temperature or the linear contribution to the total junction inductance, which is closely related to the constriction current-phase relation. We perform these analyses in more detail below and in the Supplemental Material [37].

We combine several *LC* circuits on a single coplanar waveguide feedline, more specifically four circuits with a SQUID and three circuits without a SQUID for reference. The base circuits only differ in the number of fingers in the IDCs and in the corresponding resonance frequencies between 3 and 7 GHz. We present data for three of the SQUID resonators with three different constriction types; one resonator has 2D constrictions (junction thickness

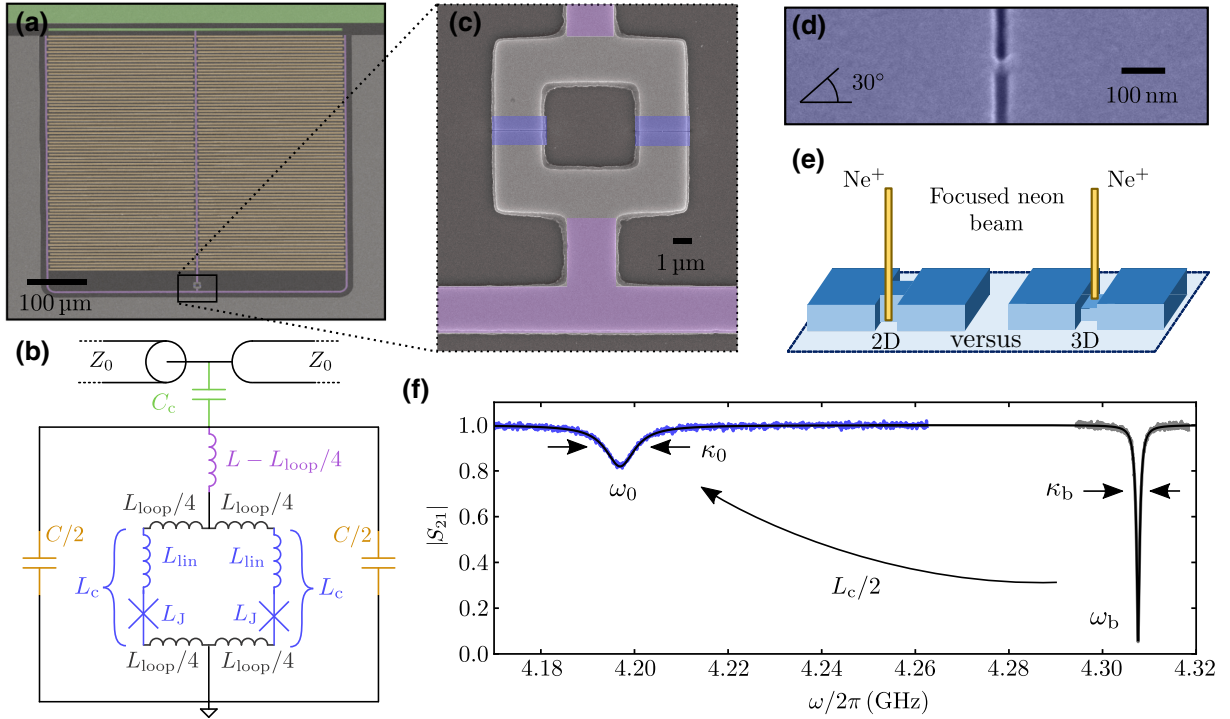


FIG. 1. A niobium-based quantum interference microwave circuit with monolithic three-dimensional nanobridge junctions. (a) False-color optical micrograph and (b) equivalent circuit of a typical device. The main circuit inductance (purple) is modeled by a linear inductor $L - L_{\text{loop}}/4$ and the two interdigitated capacitors (IDCs; orange) have a total capacitance of C . Each of the two IDCs has N_{idc} (here $N_{\text{idc}} = 46$) fingers with a length of $l = 250 \mu\text{m}$ and a width of $W = 3 \mu\text{m}$. In the center of the circuit is a loop structure for the SQUID. The square-shaped loop has a total loop inductance $L_{\text{loop}} \approx 17 \text{ pH}$ and the nanobridges (blue) have a constriction inductance L_c (only $\neq 0$ after junction patterning). The resonant circuit is capacitively coupled to a coplanar waveguide transmission line with a characteristic impedance of $Z_0 \approx 50 \Omega$ by means of a coupling capacitance C_c (coupling elements green). (c) False-color scanning electron microscopy (SEM) image of the loop after constriction cutting; (d) enlarged view of a 3D constriction after cutting, taken with a SEM tilt angle of 30° . In (a), (c), and (d) niobium is bright gray and colored. The silicon substrate is dark gray. Panel (e) schematically illustrates the nanoconstriction fabrication. For the 2D constrictions, two narrow slits are patterned into each of the SQUID arms by a neon focused ion beam; for the 3D constrictions, the nanobridges are additionally thinned down from the top by the neon beam. (f) Transmission $|S_{21}|$ of one of the circuits (device 3D₁) at $T_s = 2.5 \text{ K}$ before (gray) and after (blue) the constriction cutting; black lines are fits to the data. Before the junction cutting, the circuit has a resonance frequency ω_b and a linewidth κ_b ; after the cutting the circuit has a resonance frequency ω_0 and a linewidth κ_0 . Values can be found in the main text. From the shift of the resonance frequency induced by the cutting, we determine the total additional inductance of the constrictions $L_c/2$.

$d_{\text{JJ}} = 90 \text{ nm}$) and two resonators have 3D constrictions with $d_{\text{JJ}} \approx 30 \text{ nm}$ (3D₁) and with $d_{\text{JJ}} \approx 20 \text{ nm}$ (3D₂) (thicknesses are estimated from the neon ion dose). The chip is $10 \times 10 \text{ mm}^2$ large and is mounted onto a printed circuit board (PCB), to which both the ground planes and the coplanar waveguide feedlines are connected through wirebonds. The chip and PCB are placed in a radiation-tight copper housing and the package—including a magnet coil fixed to the box—is mounted inside the vacuum chamber of a dipstick that can be inserted into a liquid helium cryostat. The cryostat allows for high-stability temperature control in the range $2.4 < T < 7.5 \text{ K}$ by a combination of pumping on the liquid helium container and a feedback loop using a temperature diode and a heating resistor in the vacuum compartment where the sample is mounted. The sample box including the magnet is additionally placed

into a cryoperm magnetic shield and the whole cryostat is packed into a double-layer room-temperature mu-metal shield. The microwave input line is strongly attenuated by 30 dB to equilibrate the incoming noise to the sample temperature and the output line is connected to a cryogenic high-electron-mobility-transistor amplifier. More details on the experimental setup are given in Appendix B and Note I within the Supplemental Material [37].

III. IMPACT OF JUNCTION CUTTING

As first step in our device characterization, we measure the transmission coefficient S_{21} with a vector network analyzer (VNA) once before the constriction patterning and once after. For all data presented here, below, and in the Supplemental Material [37], the VNA probe tone power

is chosen to be sufficiently weak, such that all nanoconstriction circuits are always in the linear response regime. This corresponds to intracircuit probe photon numbers $n_{\text{pr}}^{2\text{D}} < 70$, $n_{\text{pr}}^{3\text{D}_1} < 10$ and $n_{\text{pr}}^{3\text{D}_2} < 2$ for all VNA measurements. In Fig. 1(f), the transmission $|S_{21}|$ at 2.5 K for device 3D₁ is shown in direct comparison for both cases. From the fits, we obtain the resonance frequencies $\omega_b = 2\pi \cdot 4.308$ GHz (no constrictions) and $\omega_0 = 2\pi \cdot 4.197$ GHz (with constrictions) and therefore we can calculate the single-constriction inductance from the constriction-induced frequency shift via

$$\omega_0 = \frac{\omega_b}{\sqrt{1 + L_c/(2L)}}. \quad (1)$$

Here and for all further analyses in this work, we assume two identical constrictions in each SQUID. Using $L = 568$ pH, as obtained from a combination of measuring the temperature dependence of the resonance frequency and numerical simulations with the software package 3D-MLSI [40] (see Note II within the Supplemental Material [37] for all device parameters), we get $L_c^{3\text{D}_1} = 61$ pH for device 3D₁.

Additionally, we extract the internal (subscript “i”) and external (subscript “e”) linewidths from the fit before and after nanobridge patterning and obtain $\kappa_{i,b} = 2\pi \cdot 73$ kHz, $\kappa_{e,b} = 2\pi \cdot 1.2$ MHz without and $\kappa_i = 2\pi \cdot 6.5$ MHz, $\kappa_e = 2\pi \cdot 1.4$ MHz with the constriction junctions. Here $\kappa_b = \kappa_{i,b} + \kappa_{e,b}$ and $\kappa_0 = \kappa_i + \kappa_e$.

The slight increase in the external linewidth could be caused by parasitic reflections in the microwave feedlines and/or cables and by the resulting partial standing wave pattern, which will lead to the input impedance of the feedline at the location of the resonator being different from 50Ω in a possibly frequency-dependent fashion. Other possible causes are parasitic signal paths, e.g., around the chip [41], leading to frequency-dependent Fano interferences and fitting errors as described in Ref. [42]. Both effects could be different before and after the Ne-FIB step due to the chip being wirebonded for a second time after the constriction nanopatterning.

The considerable increase in the internal linewidth on the other hand indicates that cutting the junction has introduced an additional loss channel and we believe that it is related to an increased quasiparticle density inside the constriction. First, it has been observed that ion-milled constrictions have a reduced critical temperature compared to the rest of the niobium film [43–46], which locally decreases the superconducting gap and increases the intrinsic thermal quasiparticle density; see also the later discussion of the temperature dependence of the devices. Based on this reduced gap, the local quasiparticle density could even be further increased, since the constriction with the reduced gap might act as a potential well or trap for thermal quasiparticles from the leads, similar to what has

been observed in aluminum constrictions or vortex cores [47,48]. We note that the increase in losses could also be partly related to generating some normal-conducting niobium at the surface or at the edges of the constriction by the neon ions. To illuminate the exact loss mechanisms in detail, however, further and dedicated experiments will be necessary in the future.

By performing completely analogous experiments and data analyses for the 2D and 3D₂ circuits (see Appendix D), we extract the corresponding constriction inductances to be $L_c^{2\text{D}} = 8$ pH and $L_c^{3\text{D}_2} = 103$ pH. More details regarding the three circuits and their basic parameters, L , C , L_{loop} , C_c , and $\kappa_{i/e}$, can be found in Note II within the Supplemental Material [37].

IV. FLUX TUNING

In order to learn more about the nature of the constrictions and how our SQUID circuits perform in terms of frequency tunability, flux responsivity, and the screening parameter, we apply an external magnetic field to the circuits that introduces magnetic flux Φ_{ext} into the SQUIDs. The constriction inductance L_c we obtained above is not necessarily a purely nonlinear Josephson inductance, but might have a linear contribution as well. In many cases, nanoconstrictions have been found to have forward-skewed sinusoidal current-phase relationships (CPRs) [33, 38,49–51] and such a skewed sine function can also be modeled approximately as a series combination of an ideal Josephson inductance L_J with sinusoidal CPR and a linear inductance L_{lin} [49], i.e., $L_c = L_J + L_{\text{lin}}$; see Fig. 2(a). Here, the ideal Josephson inductance would be given by $L_J = L_{J0}/\cos\varphi$, where φ is the phase difference across the junction, $L_{J0} = \Phi_0(2\pi I_0)^{-1}$, and I_0 is the critical current of the junction. The Josephson phase φ of each junction in a symmetric SQUID without bias current is related to the total flux Φ in the loop via $\varphi = \pi\Phi/\Phi_0$. To change the magnetic flux through the loop, we sweep a dc current through the magnet coil attached to the backside of the chip housing, which generates a nearly homogeneous out-of-plane magnetic field at the position of the SQUIDs.

Figure 2(b) shows the circuit response $|S_{21}|$ of the 3D₁ SQUID circuit for several bias fluxes Φ_{ext} . We observe that the resonance dip moves to lower frequencies, i.e., that the resonance frequency is shifted downwards with flux, and that the depth of the dip decreases while the linewidth increases, at least as long as $\Phi_{\text{ext}} < \Phi_0/2$ with the flux quantum $\Phi_0 \approx 2.068 \times 10^{-15}$ Tm². Over larger flux ranges, we in fact observe an oscillating behavior of the resonance frequency $\omega_0(\Phi_{\text{ext}})$ with a periodicity of Φ_0 , reflecting fluxoid quantization in the SQUID loop; see Fig. 2(c). Very much as suggested by previous reports [36,38] and as intuitively expected, we observe that the resonance frequency tuning range (difference

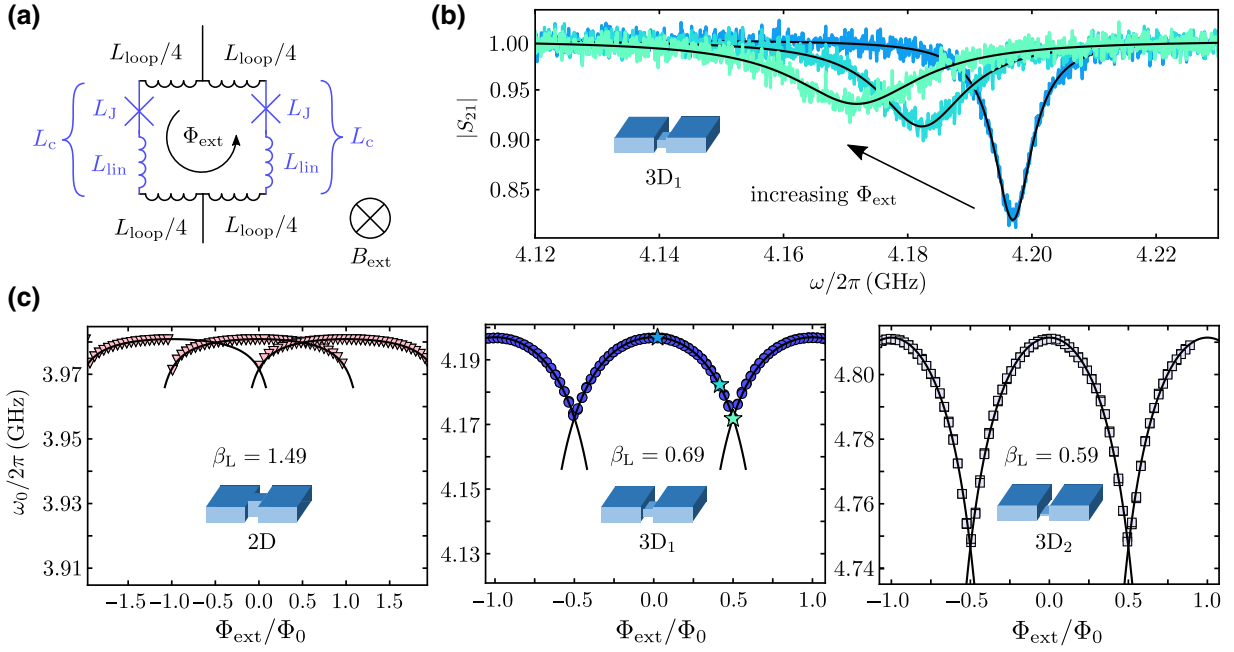


FIG. 2. Flux tuning the resonance frequency of niobium quantum interference circuits with 2D and 3D constriction junctions. (a) Circuit equivalent of the SQUID with a linear loop inductance $L_{\text{loop}}/2$ in each arm and a constriction inductance L_c , modeled by a linear contribution L_{lin} and a sinusoidal Josephson contribution L_J . We apply an external magnetic field B_{ext} perpendicular to the SQUID loop to change the inductances $L_J(\Phi_{\text{ext}})$ with the externally applied magnetic flux Φ_{ext} and with it the resonance frequency of the circuit. (b) Transmission response $|S_{21}|$ of the 3D₁ constriction SQUID circuit for three different external fluxes Φ_{ext} and $T_s = 2.5$ K. With increasing Φ_{ext} , the resonance shifts towards lower frequencies, indicating an increase in the constriction inductance by flux. Colored noisy lines are data and black smooth lines are fits. The flux values are $\Phi_{\text{ext}}/\Phi_0 = 0, 0.4, 0.5$. From the fits, we extract the resonance frequency $\omega_0(\Phi_{\text{ext}})$, which is shown as a function of flux in panel (c) for the three different circuits with three different constrictions. Insets show sketches of the junction type. Symbols are data and lines are fits from which we extract the screening parameter β_L . Left: 2D constriction with a thickness of about 90 nm. Middle: 3D constriction 3D₁ with a thickness of about 30 nm; star-shaped data points correspond to the data sets in (b). Right: 3D constriction 3D₂ with a thickness of about 20 nm. With decreasing thickness of the constriction, the tuning range gets larger and the screening parameter β_L and flux hysteresis (overlap of adjacent flux arches) decrease.

between the maximum and minimum resonance frequencies) gets larger with decreasing constriction thickness. For the 2D junctions [left plot in Fig. 2(c)], the total resonance frequency tuning range that we can achieve is only about 10 MHz and the individual flux arches strongly overlap with a total observable width of each arch of about $2\Phi_0$. For the 3D₂ device [right plot in Fig. 2(c)], the tuning range is about 65 MHz and a flux hysteresis (two possible resonance frequencies for a single flux value as in the 2D circuit) is not observable in the data. The 3D₁ circuit is somewhere in between, just as it is positioned in Fig. 2(c).

To quantitatively model the flux dependence of the resonance frequency and gather information about L_J and L_{lin} , we consider a flux-dependent resonance frequency

$$\omega_0(\Phi_{\text{ext}}) = \frac{\omega_b}{\sqrt{1 + \frac{1}{2L} \left(L_{\text{lin}} + \frac{L_{J0}}{\cos\left(\pi \frac{\Phi}{\Phi_0}\right)} \right)}}. \quad (2)$$

The relation between the total flux in the SQUID Φ and the external flux Φ_{ext} is given by

$$\frac{\Phi}{\Phi_0} = \frac{\Phi_{\text{ext}}}{\Phi_0} - \frac{\beta_L}{2} \sin\left(\pi \frac{\Phi}{\Phi_0}\right), \quad (3)$$

where

$$\beta_L = \frac{2I_0(L_{\text{loop}} + 2L_{\text{lin}})}{\Phi_0} = \frac{L_{\text{loop}} + 2L_{\text{lin}}}{\pi L_{J0}} \quad (4)$$

is the effective SQUID screening parameter. The result of fitting the flux dependence of the resonance frequency with Eqs. (2) and (3) is shown as lines in Fig. 2(c) and shows good agreement with the experimental data for all three circuits.

The fit parameters we obtain for the single-junction sweetspot inductance L_{J0} , the single-junction critical current I_0 , the linear inductance contribution L_{lin} , and the screening parameter β_L are summarized in Table I. Interestingly, the extracted inductances do not show the somewhat expected tendency that L_{lin}/L_{J0} , representing the

TABLE I. Nanobridge and SQUID parameters for the three circuits. Parameters are the same as those for the flux-tuning curve fits of Fig. 2(c) at $T_s = 2.5$ K.

Circuit	I_0 (μA)	L_{J0} (pH)	L_{lin} (pH)	β_L
2D	65	5	3	1.49
3D ₁	10	33	28	0.69
3D ₂	6	58	45	0.59

skewedness of the CPR, decreases with d_{JJ} and I_0 . As a consequence of the low critical current in the 3D₂ device, however, we obtain a small screening parameter $\beta_L = 0.59$ despite our large SQUID loop and a maximum flux responsivity $\partial\omega_0/\partial\Phi_{\text{ext}} \approx 2\pi \cdot 400$ MHz/ Φ_0 , on par with similar aluminum constriction devices [52,53] and highly promising for applications in photon-pressure systems and flux-mediated optomechanics. The screening parameters in the optimized aluminum-constriction circuits in Refs. [52,53] for 50–100- μm^2 -large SQUIDs have been obtained as $\beta_L = 0.7$ and $\beta_L = 1.1$, respectively, and the flux responsivities used in these experiments have been between $\partial\omega_0/\partial\Phi_{\text{ext}} \approx 2\pi \cdot 250$ MHz/ Φ_0 and $\partial\omega_0/\partial\Phi_{\text{ext}} \approx 2\pi \cdot 520$ MHz/ Φ_0 . Therefore, it is now possible to work with comparable circuits, responsivities, and screening parameters as before, but at a considerably higher temperature (here $T_s \sim 2.5$ K) and presumably at much larger magnetic in-plane fields. Note also that the flux responsivities strongly depend on the linear inductance of the circuit L , which is highly designable and is currently about 500 pH. With a different circuit layout such as that in, e.g., Ref. [54] and an even thicker film, L could be reduced by up to one order of magnitude, thereby also increasing the tuning range and the flux responsivity by a factor of about 5 compared to now.

Regarding the increase in the linewidth with flux, which is visible in the data of Fig. 2(b), we believe that it is related to a reduction in the superconducting gap with increasing current in the constriction [50], and the corresponding increase in local quasiparticle density, both by the reduction of the gap itself, but also by trapping more quasiparticles from the leads. Most likely, there are additional contributions due to internal and external low-frequency flux noise and thermal photon occupation of a nonlinear resonator [19], which at $T_s = 2.5$ –3.5 K is $\bar{n}_{\text{th}} \sim 10$ –20 photons for an 4–5 GHz mode based on the Bose distribution $\bar{n}_{\text{th}} = (e^{\hbar\omega_0/k_B T_s} - 1)^{-1}$.

V. TEMPERATURE DEPENDENCE

An interesting question when characterizing and operating superconducting microwave devices and SQUIDs at a temperature several tens of percent of the critical temperature T_c is how the properties depend on the sample temperature T_s in that regime and if we can extrapolate to the properties at lower temperatures from that. The most

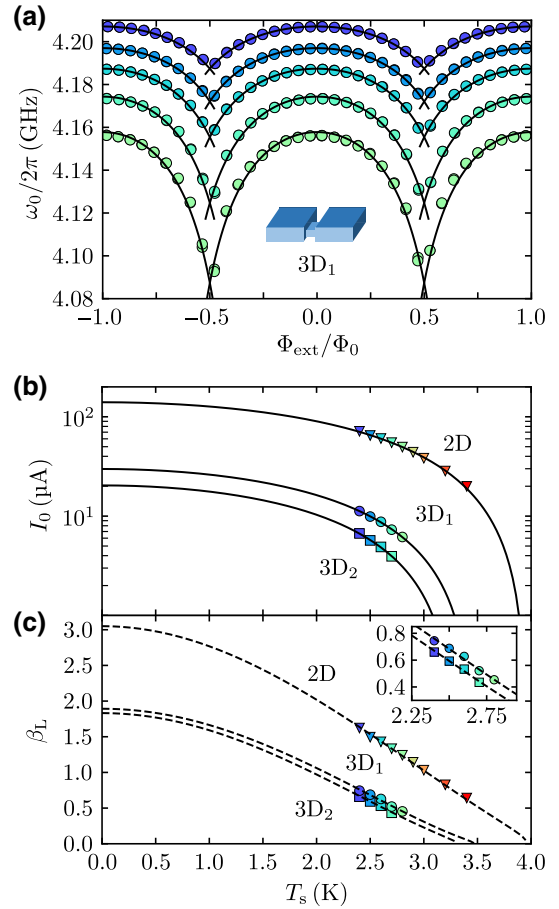


FIG. 3. Temperature dependence of the circuit and SQUID. (a) Flux-tuning curve $\omega_0(\Phi_{\text{ext}})$ of device 3D₁ for several different sample temperatures $T_s = 2.4$ –2.8 K in steps of 0.1 K. Top curve: lowest temperature. Bottom curve: highest temperature. Circles are data and lines are fits to Eqs. (2) and (3). From the fits we extract the critical current of the constriction I_0 and the screening parameter β_L ; the obtained values for both are shown as circles in (b) and (c), respectively. (b) Critical current I_0 versus the sample temperature T_s for all three constriction SQUID cavities as extracted from the corresponding flux-tuning curves. Symbols are data and lines are fits. From the theoretical fit curves (see the main text), we can extrapolate to the critical current at millikelvin temperatures and obtain the critical temperatures of the constrictions $T_{\text{cc}}^{2\text{D}} = 3.96$ K, $T_{\text{cc}}^{3\text{D}1} = 3.47$ K, and $T_{\text{cc}}^{3\text{D}2} = 3.31$ K. In combination with the temperature dependencies of L_{loop} and L_{lin} , we can calculate theoretical lines for $\beta_L(T_s)$, as shown in panel (c), for all three circuits in comparison to the experimental data. Inset shows an enlarged view of the data for the 3D samples.

relevant parameters we are going to consider here are the cavity resonance frequency $\omega_0(T_s)$, the constriction critical current $I_0(T_s)$, and the SQUID screening parameter $\beta_L(T_s)$ for all three circuits.

The main results are summarized in Fig. 3. We repeat the experiment of flux tuning presented in the previous section for different sample temperatures T_s . From the transmission curves S_{21} for varying external flux we extract

$\omega_0(T_s, \Phi_{\text{ext}})$ [see Fig. 3(a) for a corresponding dataset of sample 3D₁]. Corresponding datasets for 2D and 3D₂ can be found in Appendix D. For each temperature T_s , we also measured $\omega_b(T_s)$, so we have a reference resonance frequency from before neon irradiation; see also Note II within the Supplemental Material [37] for the temperature dependence of the constrictionless 3D₁.

We observe in the resonance frequency tuning curves that with decreasing temperature the zero-flux resonance frequency gets shifted to larger values, a clear indication for a reduction of the kinetic inductance both in the constrictions and in the rest of the circuit. Furthermore, we find that the tuning range of the resonance frequency grows with increasing temperature, indicating that the constriction inductance increases faster than the remaining circuit inductance, and we observe that the screening parameter β_L decreases, since L_{J0} is increasing faster with T_s than the effective loop inductance $L_{\text{loop}} + 2L_{\text{lin}}$.

For a quantification of these effects, we fit the flux-tuning data again with the same equations and procedure as described in the previous section. As a result, we obtain for each sample $L_{J0}(T_s)$ and $L_{\text{lin}}(T_s)$ (see Note V within the Supplemental Material [37]), and from the former we calculate $I_0(T_s) = \Phi_0[2\pi L_{J0}(T_s)]^{-1}$. The critical currents obtained from this are shown for all three circuits in Fig. 3(b). We model the data with the theoretical Bardeen expression for the critical current of a constriction [44,55]

$$I_0(T_s) = I_c \left[1 - \left(\frac{T_s}{T_{\text{cc}}} \right)^2 \right]^{3/2}, \quad (5)$$

and find as fitting parameters the critical current at zero temperature I_c as well as the constriction critical temperature T_{cc} . As we have already speculated above, the critical temperature T_{cc} of the constrictions is considerably reduced compared to the niobium film to values between $T_{\text{cc}}^{2\text{D}} = 3.96$ K and $T_{\text{cc}}^{3\text{D}2} = 3.31$ K according to these fits. Interestingly, similar T_{cc} values have also been observed for electron-beam-patterned niobium nanobridges with comparable critical currents [44]; therefore, the reduced transition temperature might not actually be related to an impact of the neon ions. Since according to this fit our data are taken at $T_s > 0.5T_{\text{cc}}$, we find that the critical currents still increase by a factor of 2 in the 2D constrictions and by about a factor of 3 in the 3D constrictions when approaching $T_s \rightarrow 0$ and with respect to the smallest experimental temperature $T_s^{\text{min}} = 2.4$ K.

It is also interesting to discuss the temperature dependence of β_L and its projected values in the millikelvin regime, although this is a bit speculative due to the limited range of data available. The experimental data shown in Fig. 4(c) for all three circuits have been obtained from the flux-tuning fits. For the 2D sample, the values for β_L are found to be between 0.6 and 1.6 in the measured regime and, for the 3D samples, between 0.4 and 0.8. To

model the temperature dependence, we take into account the fit curves for $I_0(T_s)$ as shown in panel (b), the temperature dependence of the loop inductance $L_{\text{loop}}(T_s)$ as discussed in Note II within the Supplemental Material [37], and the temperature dependence of $L_{\text{lin}}(T_s)$ that we obtain by a fit of the experimentally obtained values (see Note V within the Supplemental Material [37]). We find curves that coincide very well with the experimental data in the measured range of T_s and that predict screening parameters for $T_s \rightarrow 0$ saturating around 3.1 for the 2D constrictions and around 1.8 and 1.9 for the 3D SQUIDs. All these values are still smaller than or comparable to the millikelvin screening parameter $\beta_L > 3.4$ given in Ref. [30] for 2D niobium constrictions, despite the fact that our SQUID areas are almost a factor 20 larger.

It seems that the nonsinusoidal CPR of the constrictions is currently the main limiting factor for β_L in the 3D samples, while in the 2D sample $2L_{\text{lin}}^{2\text{D}} \approx 6$ pH and the screening parameter is limited by the actual L_{loop} . It will be interesting to see in future experiments in the millikelvin temperature regime if these predictions are valid or if so-far neglected effects will emerge and lead to a different behavior than expected. With lower-temperature experimental possibilities, it will also be interesting to further reduce the thickness and critical current of the 3D junctions, which in the current setup with $T_s^{\text{min}} \approx 2.4$ K was not possible, as can be seen from the very limited temperature range already accessible in the existing 3D devices with $T_{\text{cc}} < 3.5$ K.

VI. KERR NONLINEARITY OF THE CIRCUITS

As a final experiment, we determine a very important parameter of Josephson-based microwave circuits—their Kerr constant \mathcal{K} , also called the anharmonicity or Kerr nonlinearity, which is equivalent to the circuit resonance frequency shift per intracavity photon. For many applications, a small Kerr nonlinearity is highly desired, as it increases the dynamic range or maximum intracavity photon number of the device. This is important, for instance, in parametric amplifiers [5–7,56] and in cavity-based detection techniques such as dispersive SQUID readout [8,9,54], SQUID optomechanics [15,57], and photon-pressure sensing [11,12], where the signal of interest is proportional to the intracavity photon number n_c and therefore profits from high-power detection tones. The origin of the nonlinearity in our SQUID circuits is the nonlinear inductance of the nanoconstrictions. In order to access \mathcal{K} experimentally, we implement a two-tone protocol, (see, e.g., Refs. [56,58]), and measure the equivalent of the ac Stark shift in the driven circuits. The first microwave tone of the two-tone scheme is a fixed-frequency pump tone with variable power P_p and a frequency ω_p slightly blue detuned from the undriven cavity resonance $\omega_p = \omega_0 + \Delta_p$ with $\Delta_p \sim \kappa$. For each pump power, we then measure the

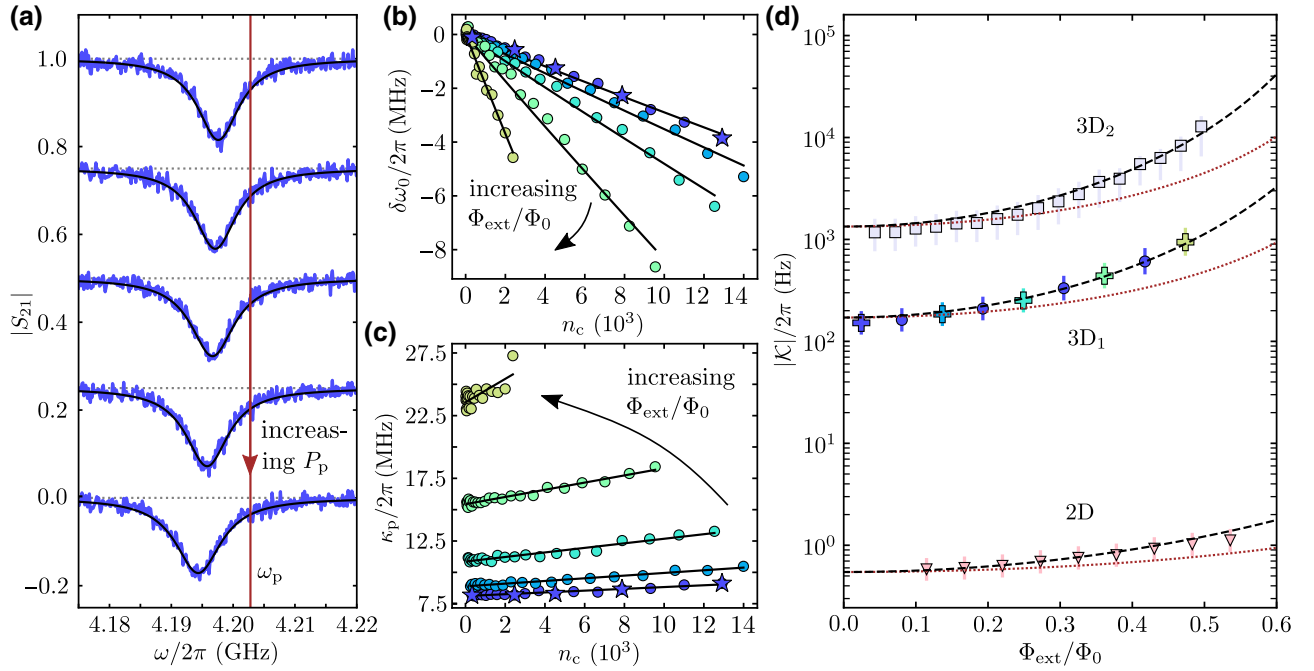


FIG. 4. Two-tone characterization of the SQUID-circuit Kerr nonlinearity. (a) The SQUID circuit transmission response S_{21} is probed with a weak microwave signal, while a strong microwave pump tone with fixed frequency ω_p and variable power P_p is applied slightly blue detuned from the cavity resonance $\omega_p - \omega_0 = \Delta_p \sim \kappa$. With increasing P_p , the dressed circuit resonance frequency shifts towards lower frequencies and the linewidth increases. Five datasets for five different P_p are shown; subsequent datasets are offset by -0.25 for clarity. From fits (black lines) to the data (blue noisy lines) we calculate the resonance frequency shift $\delta\omega_0 = \omega_0(P_p) - \omega_0(0)$ and the linewidth κ_p . The results are shown in panels (b) and (c) for different Φ_{ext} , temperature $T_s = 2.5$ K, and sample $3D_1$. Circles are data and lines are fits. Star symbols are data points that correspond to the five datasets shown in panel (a). From the fits, we determine the Kerr nonlinearity $\mathcal{K}(\Phi_{\text{ext}})$. We perform this characterization for all three circuits; the result is shown in panel (d) versus the external flux bias Φ_{ext}/Φ_0 . Symbols are data and dashed lines are theoretical curves based on the flux-tuning curve and Eq. (9), but without free parameters. Dotted red lines are theoretical curves without the correction factor arising from $\beta_L \neq 0$. Cross symbols in the data of $3D_1$ correspond to the extracted values from the datasets shown in panels (b) and (c). Error bars take into account uncertainties in the intracavity photon number n_c ; see Note VI within the Supplemental Material [37].

pump-dressed device transmission S_{21} with a small probe tone; see Fig. 4(a).

What we find qualitatively in this experiment is that, with increasing pump power, the dressed circuit resonance frequency shifts towards lower frequencies and that the internal linewidth of the mode increases; see Fig. 4(a). For a quantitative analysis, we fit each pump-dressed resonance with a linear cavity response for S_{21} (see Appendix C and Note IV within the Supplemental Material [37]), from which we extract the pump-shifted resonance frequency ω'_0 and the pump-broadened total linewidth κ_p .

To model the circuit and the results and to extract \mathcal{K} , we use the equation of motion for the complex intracavity field α :

$$\dot{\alpha} = \left[i(\omega_0 + \mathcal{K}|\alpha|^2) - \frac{\kappa_0 + \kappa_{\text{nl}}|\alpha|^2}{2} \right] \alpha + i\sqrt{\frac{\kappa_c}{2}} S_{\text{in}} \quad (6)$$

with a nonlinear damping parameter κ_{nl} , the total input field S_{in} , and a normalization such that $|\alpha|^2 = n_c$ is the total intracircuit photon number. In the linearized two-tone

regime (pump power \gg probe power; see Appendix C for details), for the pump-broadened linewidth and the pump-induced frequency shift $\delta\omega_0 = \omega_0 - \omega'_0$, we find the relations

$$\kappa_p = \kappa_0 + 2\kappa_{\text{nl}}n_c, \quad (7)$$

$$\delta\omega_0 = \Delta_p - \sqrt{(\Delta_p - \mathcal{K}n_c)(\Delta_p - 3\mathcal{K}n_c) - \frac{\kappa_{\text{nl}}^2 n_c^2}{4}}. \quad (8)$$

Subsequently, we use the $\delta\omega_0$ and κ_p as obtained from the measurements to determine the intracavity photon number n_c for each P_p without any knowledge of \mathcal{K} ; see Appendix C, in particular Eq. (C25). In Figs. 4(b) and 4(c), the extracted values $\delta\omega_0$ and κ_p are shown for various bias flux values and plotted versus the intracircuit pump photon number n_c in device $3D_1$ at a sample temperature $T_s = 2.5$ K. Both quantities show a nearly linear dependence on the pump photon number as implemented by our model and the corresponding slope depends in turn on the bias flux

Φ_{ext} . We fit the data using Eqs. (7) and (8) and obtain $\mathcal{K}(\Phi_{\text{ext}})$ for all three devices.

For all circuits, the nonlinearity shown in Fig. 4(d) increases with increasing flux, but the absolute values differ by several orders of magnitude. While the 2D circuit has a Kerr constant of about only 1 Hz, the 3D circuits possess nonlinearities of 10^2 to 10^3 Hz in 3D₁ and up to 10^3 to 10^4 Hz in 3D₂. All nonlinearities can still be considered small though and are in particular several orders of magnitude smaller than the cavity linewidths $\mathcal{K} \ll \kappa_0$. We also observe very good agreement with the theoretical expression for the Kerr nonlinearity

$$\mathcal{K} = -\frac{e^2}{2\hbar C_{\text{tot}}} \left(\frac{L_J}{2L + L_{\text{lin}} + L_J} \right)^3 \left[1 + 3\Lambda \tan^2 \left(\pi \frac{\Phi}{\Phi_0} \right) \right] \quad (9)$$

with electron charge e , total circuit capacitance $C_{\text{tot}} = C + C_c$, reduced Planck constant \hbar , and $\Lambda = (L_{\text{lin}} + L_{\text{loop}}/2)/(L_{\text{lin}} + L_{\text{loop}}/2 + L_J)$. Note that we apply the method of nonlinear current conservation discussed in Ref. [56] to obtain this theoretical expression; see Appendix E. The unusual \tan^2 term in the square brackets of Eq. (9) is, however, not stemming from an asymmetry or a hidden third-order nonlinearity, it is a correction factor for perfectly symmetric SQUIDs with screening parameter $\beta_L > 0$. How necessary it is to consider this extra term is revealed by the difference to the simple participation ratio expression [Eq. (9) with $\Lambda = 0$], which is also shown in Fig. 4(d) as dotted lines and that, for large flux bias values, differs from the exact result and the data by up to a factor of about 4. The excellent agreement between the data and the theory curves also supports our initial assumption of (nearly) identical constrictions in each SQUID, since a junction asymmetry would lead to the flux-tuning curves of either the resonance frequency or the Kerr anharmonicity to deviate from the theory assuming symmetric SQUIDs.

VII. DISCUSSION

In summary, we have reported niobium-based superconducting quantum interference microwave circuits with integrated, monolithically fabricated 2D and 3D nanoconstriction SQUIDs. The successful implementation of 3D constrictions nanopatterned with a Ne FIB constitutes a promising addition to the notoriously difficult patterning methods of such devices, and can also be applied to other materials such as aluminum or niobium alloys in the future. Our experimental results revealed that the tuning range and the flux responsivity of the circuits increase with decreasing constriction thickness and critical current. Strikingly, our circuits can be operated at temperatures up to about 4 K though, nearly an order-of-magnitude enhancement over comparable aluminum realizations. The critical currents we obtained strongly depend on constriction type

and thickness as well as on sample temperature, and we found values between $I_{0,\text{min}} \sim 4 \mu\text{A}$ and $I_{0,\text{max}} \sim 80 \mu\text{A}$ in the investigated temperature range. We believe that in the future we can even achieve critical currents as low as $1 \mu\text{A}$, possibly even in the millikelvin regime. We have also extracted and modeled the Kerr anharmonicity of all circuits and found values between 0.5 Hz for the 2D circuits and 10 kHz for the 3D circuit with the lowest critical current junctions. The overall characteristics of the circuits make them highly promising candidates for quantum circuit and quantum sensing applications, in particular when a high dynamic range and high magnetic fields will be important such as in spin-qubit circuit quantum electrodynamics, hybrid quantum devices with magnonic oscillators, dispersive magnetometry, or flux-mediated optomechanics.

Depending on the exact requirements of each hybrid system and experiment, the parameters of the embedding circuits can be easily adjusted in the future to obtain much larger (or smaller) frequency tuning ranges, larger (or smaller) flux responsivities, and larger (or smaller) Kerr nonlinearities. A good example for how strongly the embedding circuit impacts these properties is given in Ref. [54], where two very different resulting circuits are obtained from identical aluminum constriction SQUIDs by just choosing very different values for C and L . One of the circuits can be flux tuned by about 2 GHz, while the other has a tuning range of about 90 MHz. Using similar approaches and combining them with the possibility to adjust the SQUID size, the desired critical currents, and the operation temperature by at least one order of magnitude opens a very large parameter space for the design of nonlinearities, flux tunabilities, and responsivities.

The most interesting open questions to be investigated in future experiments are the circuit characteristics at temperatures in the millikelvin regime and in large magnetic fields, the exact origin of the microwave losses in the nanoconstriction circuits, and possibilities to reduce them, as well as a theoretical and experimental investigation of the noise characteristics in such devices. Finally, it will be interesting to investigate possibilities to further reduce the critical currents and the screening parameters, by potentially further reducing the size of the nanoconstrictions in all three dimensions.

All data presented in this paper and the corresponding processing scripts used during the analysis are publicly available online [59].

ACKNOWLEDGMENTS

We gratefully acknowledge technical support by M. Turad and R. Löffler (both LISA⁺) and by C. Back. We acknowledge funding by the Deutsche Forschungsgemeinschaft (DFG) via Grants No. BO 6068/1-1, No. BO 6068/2-1, and No. KO 1303/13-2, and support from

the COST actions NANOCOBYBRI (CA16218) and SUPERQUMAP (CA21144). J.P. acknowledges support from the Cusanuswerk, Bischöfliche Studienförderung.

APPENDIX A: DEVICE FABRICATION

In this appendix, the sample fabrication is described step by step, and a schematic representation of the nanoconstriction fabrication based on Ne-FIB milling is shown in Fig. 5.

Step 1: microwave cavity patterning. The fabrication starts with sputtering 90-nm niobium (Nb) on top of a high-resistivity ($\rho > 10 \text{ k}\Omega \text{ m}$) intrinsic 2-in. silicon wafer. The wafer thickness is 500 μm . Then, the complete wafer is covered with a 600-nm-thick layer of ma-P 1205 photoresist by spin coating and structured by means of maskless scanning laser photolithography ($\lambda_{\text{Laser}} = 365 \text{ nm}$). After development of the resist in ma-D 331/S for 40 s, the patterned side of the wafer is etched by means of reactive ion etching using SF_6 . For cleaning, the wafer is finally rinsed in multiple subsequent baths of acetone and isopropanol.

Step 2: dicing and mounting for precharacterization. At the end of the microwave cavity fabrication, the wafer is diced into individual $10 \times 10 \text{ mm}^2$ chips. These chips are individually mounted onto a PCB, where they are wirebonded to microwave feedlines and ground, and the complete set of chip and PCB is packaged into a radiation-tight copper housing. After mounting into the measurement setup, the precharacterization of the device is performed.

Step 3: 2D and 3D constriction fabrications. Each precharacterized LC circuit contains a square-shaped Nb loop structure with inner dimensions of $6 \times 6 \mu\text{m}^2$ and a conductor strip width of 3 μm ; see Fig. 1. Two nanoconstrictions are patterned into the opposite sides of the loops using the focused ion beam of a neon ion microscope (NIM). The NIM allows for high-precision milling with a nanoscaled spot-size Ne FIB. For the 2D constrictions, two approximately 20-nm-narrow slot-shaped rectangles are ion milled simultaneously from both sides into each loop strip with a dose of 20 000 ions/ nm^2 and an accelerating voltage of 20 kV. Simultaneous here means that the neon beam is scanned in a pattern that alternates repeatedly between the left and the right slots. In between the two slots, a milling gap of 40 nm is left untouched, where the 2D constriction is formed. The 3D constriction patterning is performed in the same way, but additionally and again simultaneously to the slot rectangles the constriction is milled from the top with a third rectangle, but with a lower ion dose. The exact value of the constriction dose defines its remaining thickness. For the 3D₁ and 3D₂ samples, the doses were 7500 and 8500 ions/ nm^2 , respectively.

Step 4: device mounting. After the Ne-FIB cutting process the sample is mounted in the same way as in step 2.

APPENDIX B: MEASUREMENT SETUP

Both the junctionless circuits and the SQUID cavities, here generically labeled as the devices under test (DUTs), are characterized in an evacuated sample space located at the end of a cryostat dipstick, which is introduced into

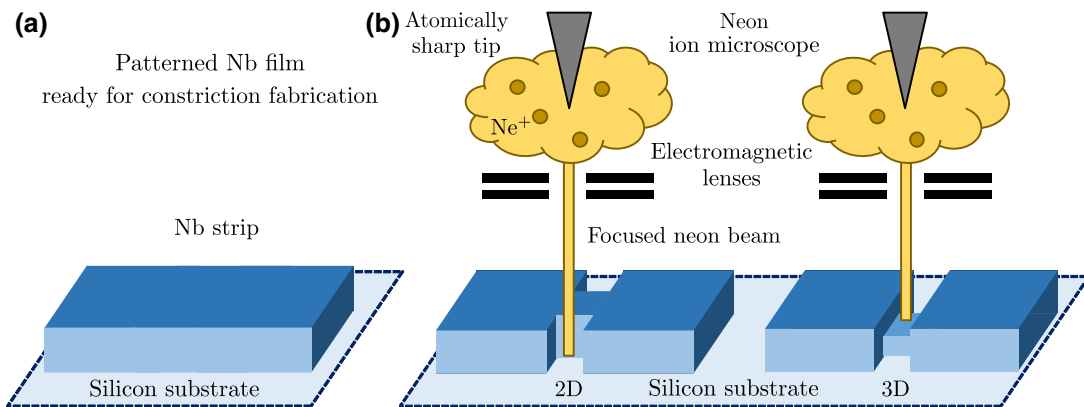


FIG. 5. Schematic niobium nanoconstriction fabrication using a neon focused ion beam. (a) Niobium (Nb) strip on a silicon substrate prepared for cutting a nanoconstriction into it. (b) Fabrication of the two different constriction types discussed in this study using a neon ion microscope (NIM): left, 2D constriction; right, 3D constriction. The NIM has an atomically sharp beam source (tip) maintained at a high voltage of 20 kV. Neon gas around the tip gets ionized and the ions are accelerated and focused through several electromagnetic lenses to form a Ne FIB with a nanoscaled spot size (about 0.5 nm). For the 2D constrictions, the strip is patterned by cutting two narrow slots from both sides into the strip. Therefore, the nanobridge has the same height as the remaining niobium leads. For the 3D constrictions, the constriction is also milled and thinned down from the top simultaneously with the slot cutting, just with a smaller ion dose.

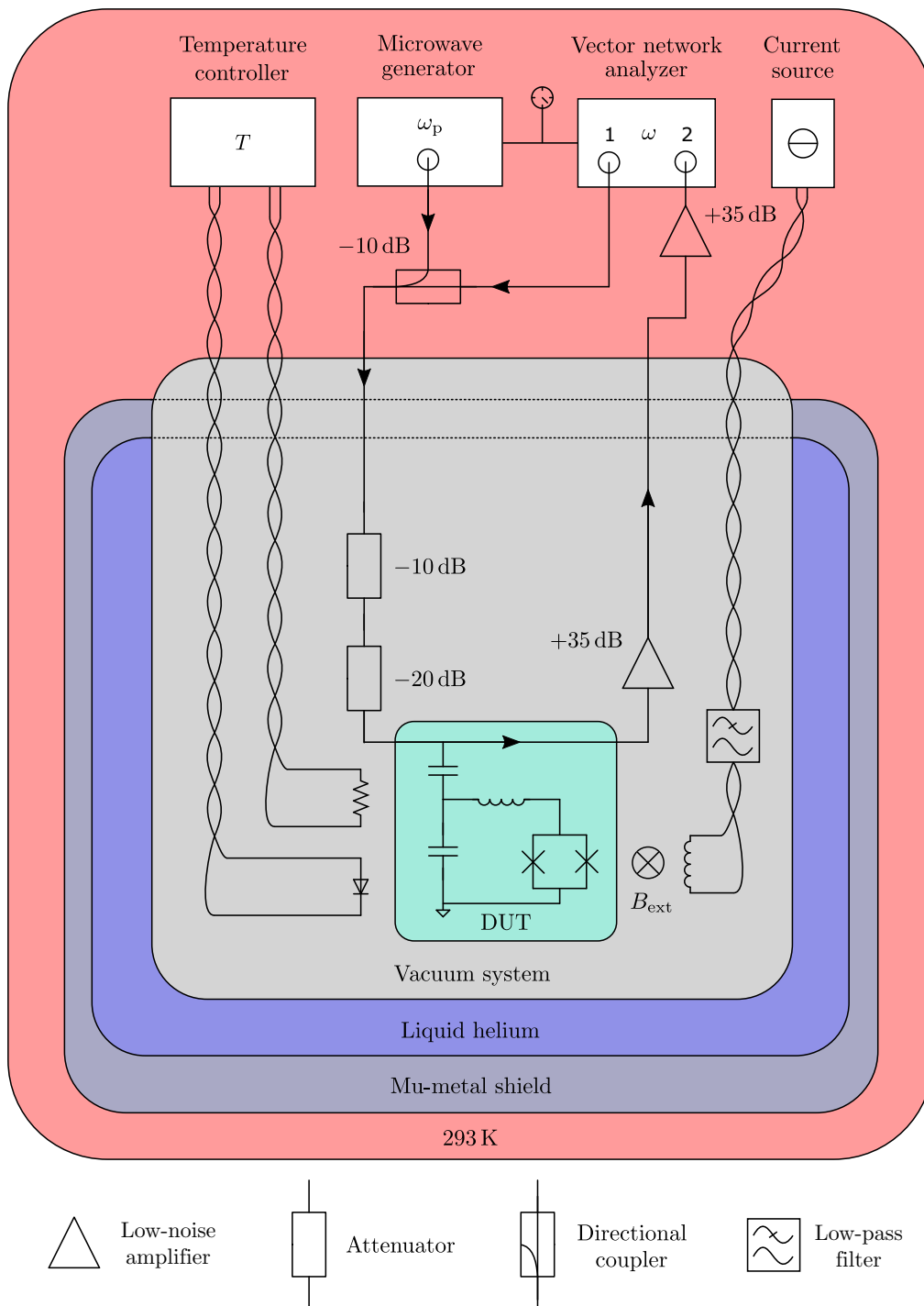


FIG. 6. Schematic of the measurement setup. In the drawing, the isolation vacuum shield in between the helium container and the outer world is omitted. Detailed information is given in the text.

a liquid helium cryostat. The cryostat is covered by a double-layer room-temperature mu-metal shield to provide magnetic shielding for the whole sample space. A schematic illustration of the measurement setup is shown in Fig. 6. The DUT inside the copper housing is attached to a copper mounting bracket and a magnet coil for the

application of a magnetic field perpendicular to the chip surface B_{ext} . The magnet coil is connected to a low-noise current source at room temperature with a twisted pair of copper wires. The magnet wires are low-pass filtered at cryogenic temperature with a cutoff frequency at about 3 kHz. Additionally, the DUT is connected to two coaxial

lines for input and output of the microwave signals. A temperature diode is attached to the sample housing in close proximity to the sample and both are coupled to the liquid helium bath via the copper mounting bracket and through helium exchange gas. For controlling the sample temperature T_s , the diode is glued with varnish to the DUT copper housing and a manganin heating resistor (made of a twisted wire pair to avoid stray magnetic fields) is placed nearby. Both the temperature diode (four wires) and the heating resistor (two wires) are also connected via twisted pairs of copper wire to a temperature controller.

The SQUID cavities are designed in a side-coupled geometry. Therefore, the input and output signals are sent and received through two separate coaxial lines in order to measure the transmission spectrum S_{21} of the DUT by a VNA. The input line is attenuated by -30 dB in order to balance the thermal radiation from room temperature to the cryostat temperature. The attenuators are mounted in close proximity to the sample in the sample vacuum space and we assume that they have a temperature $T_{\text{att}} \approx T_s$. For amplification of the weak microwave signal used here, a cryogenic high-electron-mobility-transistor (HEMT) amplifier and a room-temperature amplifier are mounted in the output line. The cryogenic HEMT is placed close to the DUT in order to minimize signal losses in between the sample and the amplifier chain.

For the two-tone experiment, an additional fixed-frequency microwave pump tone with frequency ω_p and power P_p is sent to the DUT. This pump tone is generated by a microwave generator and combined via a 10-dB directional coupler with the VNA signal before entering the cryostat. In the experiment the VNA and microwave generator are both referenced to the 10-MHz clock of the generator.

For cooling the device to temperatures below that of liquid helium $T_{\text{He}} = 4.2$ K, we pump at the helium dewar of the cryostat and reach down to $T_{s,\text{min}} \lesssim 2.4$ K with the current setup. To achieve high-stability ($\Delta T_s < 1$ mK) temperature control in the most relevant range for this work, $2.4 \lesssim T_s \lesssim 3.5$ K, we use the helium pumping and additionally heat the sample with the heating resistor whose power is controlled via a proportional–integral–derivative feedback loop by the temperature controller.

APPENDIX C: CIRCUIT RESPONSE MODEL

1. Equation of motion and general considerations

We model the classical intracavity field α of the SQUID circuits with Kerr nonlinearity and nonlinear damping using the equation of motion [28,60]

$$\dot{\alpha} = \left[i(\omega_c + \mathcal{K}|\alpha|^2) - \frac{\kappa + \kappa_{\text{nl}}|\alpha|^2}{2} \right] \alpha + i\sqrt{\frac{\kappa_e}{2}} S_{\text{in}}. \quad (\text{C1})$$

Here, ω_c is the cavity resonance frequency ($= \omega_b$ before cutting and $= \omega_0$ after), \mathcal{K} is the Kerr nonlinearity (frequency shift per photon), κ is the bare total linewidth ($= \kappa_b$ before cutting and $= \kappa_0$ after), κ_{nl} is the nonlinear damping constant, κ_e is the external linewidth ($= \kappa_{e,b}$ before cutting), and S_{in} is the input field. The intracavity field is normalized such that $|\alpha|^2 = n_c$ corresponds to the intracavity photon number n_c and $|S_{\text{in}}|^2$ to the input photon flux (photons per second) on the coplanar waveguide feedline.

The solution of this equation of motion significantly depends on the pump power and the number of tones sent to the cavity. The ideal transmission response function, however, will always be of the form

$$S_{21}^{\text{ideal}} = 1 + i\sqrt{\frac{\kappa_e}{2}} \frac{\alpha}{S_{\text{in}}} \quad (\text{C2})$$

with the solution of interest α .

2. The linear single-tone regime

In the linear single-tone regime, we set $\mathcal{K} = \kappa_{\text{nl}} = 0$. Then, we can solve the remaining equation by Fourier transformation and obtain

$$\alpha = \frac{i\sqrt{\kappa_e/2}}{\kappa/2 + i(\omega - \omega_c)} S_{\text{in}}. \quad (\text{C3})$$

The ideal transmission response of a capacitively side-coupled and linear LC circuit is then given by

$$S_{21}^{\text{ideal}} = 1 - \frac{\kappa_e}{\kappa + 2i(\omega - \omega_c)}. \quad (\text{C4})$$

3. The nonlinear single-tone regime

In the nonlinear single-tone regime, we have to solve the full equation of motion and start by setting the input field to $S_{\text{in,st}} = S_0 e^{i\phi_p} e^{i\omega t}$ with real valued S_0 . For the intracavity field, we make the ansatz $\alpha(t) = \alpha_0 e^{i\omega t}$ with real valued α_0 . The phase delay between input and response is encoded in ϕ_p . Then the equation of motion reads

$$i\omega\alpha_0 = \left[i(\omega_c + \mathcal{K}\alpha_0^2) - \frac{\kappa + \kappa_{\text{nl}}\alpha_0^2}{2} \right] \alpha_0 + i\sqrt{\frac{\kappa_e}{2}} S_0 e^{i\phi_p}, \quad (\text{C5})$$

which after multiplication with its complex conjugate yields the characteristic polynomial for the intracircuit photon number $n_c = \alpha_0^2$:

$$n_c^3 \left[\mathcal{K}^2 + \frac{\kappa_{\text{nl}}^2}{4} \right] + n_c^2 \left[\frac{\kappa\kappa_{\text{nl}}}{2} - 2\mathcal{K}\Delta \right] + n_c \left[\Delta^2 + \frac{\kappa^2}{4} \right] - \frac{\kappa_e}{2} S_0^2 = 0. \quad (\text{C6})$$

Here $\Delta = \omega - \omega_c$ is the detuning between the microwave input tone and the bare cavity resonance. The real-valued

roots of this polynomial correspond to the physical solutions for the amplitude α_0 ; the highest and lowest amplitudes are the stable states in the case of three real-valued roots.

For the complete complex transmission, we also need the phase ϕ_p , which we obtain via

$$\phi_p = \text{atan2}\left(-\frac{\kappa + \kappa_{\text{nl}}n_c}{2}, \Delta - \mathcal{K}n_c\right). \quad (\text{C7})$$

Having both parts of the complex field solution at hand, we can also calculate the transmission

$$S_{21,\text{nl}}^{\text{ideal}} = 1 + i\sqrt{\frac{\kappa_e}{2}}\frac{\alpha_0}{S_0}e^{-i\phi_p}. \quad (\text{C8})$$

Note that we do not use these equations for any data analysis in this manuscript, but we include them for pedagogical reasons, since they facilitate understanding the two-tone regime.

4. The linearized two-tone regime

In the two-tone experiments, we apply a strong pump tone with fixed frequency ω_p and fixed power P_p and probe the cavity response with a weak additional scanning tone; the total input is then $S_{\text{in,tt}} = S_0 e^{i\phi_p} e^{i\omega_p t} + S_{\text{pr}}(t) e^{i\omega_p t}$. The probe input amplitude $S_{\text{pr}}(t)$ is time dependent and complex valued. As an ansatz for the intracavity field, we choose $\alpha(t) = \alpha_0 e^{i\omega_p t} + \alpha_{\text{pr}}(t) e^{i\omega_p t}$ with a complex and time dependent $\alpha_{\text{pr}}(t)$ and obtain the equation of motion

$$\begin{aligned} & i\omega_p \alpha_0 + i\omega_p \alpha_{\text{pr}} + \dot{\alpha}_{\text{pr}} \\ &= i[\omega_c + \mathcal{K}(\alpha_0^2 + \alpha_0(\alpha_{\text{pr}} + \alpha_{\text{pr}}^*) + |\alpha_{\text{pr}}|^2)]\alpha_0 \\ &+ i[\omega_c + \mathcal{K}(\alpha_0^2 + \alpha_0(\alpha_{\text{pr}} + \alpha_{\text{pr}}^*) + |\alpha_{\text{pr}}|^2)]\alpha_{\text{pr}} \\ &- \left[\frac{\kappa}{2} + \frac{\kappa_{\text{nl}}}{2}(\alpha_0^2 + \alpha_0(\alpha_{\text{pr}} + \alpha_{\text{pr}}^*) + |\alpha_{\text{pr}}|^2)\right]\alpha_0 \\ &- \left[\frac{\kappa}{2} + \frac{\kappa_{\text{nl}}}{2}(\alpha_0^2 + \alpha_0(\alpha_{\text{pr}} + \alpha_{\text{pr}}^*) + |\alpha_{\text{pr}}|^2)\right]\alpha_{\text{pr}} \\ &+ i\sqrt{\frac{\kappa_e}{2}}S_0 e^{i\phi_p} + i\sqrt{\frac{\kappa_e}{2}}S_{\text{pr}}. \end{aligned} \quad (\text{C9})$$

Now we perform the linearization, i.e., we drop all terms not linear in the small quantity α_{pr} and get

$$\begin{aligned} & i\omega_p \alpha_0 + i\omega_p \alpha_{\text{pr}} + \dot{\alpha}_{\text{pr}} \\ &= \left[i(\omega_c + \mathcal{K}n_c) - \frac{\kappa + \kappa_{\text{nl}}n_c}{2} \right] \alpha_0 \end{aligned}$$

$$\begin{aligned} & + \left[i(\omega_c + 2\mathcal{K}n_c) - \frac{\kappa + 2\kappa_{\text{nl}}n_c}{2} \right] \alpha_{\text{pr}} \\ & + \left[i\mathcal{K} - \frac{\kappa_{\text{nl}}}{2} \right] n_c \alpha_{\text{pr}}^* + i\sqrt{\frac{\kappa_e}{2}}S_0 e^{i\phi_p} + i\sqrt{\frac{\kappa_e}{2}}S_{\text{pr}}. \end{aligned} \quad (\text{C10})$$

The time-independent terms are identical to Eq. (C6) of the nonlinear single-tone experiment and allow one to determine α_0 and n_c via the characteristic polynomial now. The remaining equation can be Fourier transformed to give

$$\frac{\alpha_{\text{pr}}}{\chi_{\text{pr}}} = \left[i\mathcal{K} - \frac{\kappa_{\text{nl}}}{2} \right] n_c \bar{\alpha}_{\text{pr}} + i\sqrt{\frac{\kappa_e}{2}}S_{\text{pr}}, \quad (\text{C11})$$

where

$$\chi_{\text{pr}} = \frac{1}{(\kappa + 2\kappa_{\text{nl}}n_c)/2 + i(\Delta_p - 2\mathcal{K}n_c + \Omega)} \quad (\text{C12})$$

with $\bar{\alpha}_{\text{pr}} = \alpha_{\text{pr}}^*(-\Omega)$, the detuning between the pump and bare cavity resonance $\Delta_p = \omega_p - \omega_c$, and the probe frequency with respect to the pump $\Omega = \omega - \omega_p$.

Using the equivalent equation for $\bar{\alpha}_{\text{pr}}$ with $\bar{S}_{\text{pr}} = 0$, we get

$$\alpha_{\text{pr}} = i\chi_g \sqrt{\frac{\kappa_e}{2}}S_{\text{pr}} \quad (\text{C13})$$

with

$$\chi_g = \frac{\chi_{\text{pr}}}{1 - [\mathcal{K}^2 + \kappa_{\text{nl}}^2/4]n_c^2 \chi_{\text{pr}} \bar{\chi}_{\text{pr}}}, \quad (\text{C14})$$

and, for the two-tone transmission parameter,

$$S_{21,\text{tt}}^{\text{ideal}} = 1 - \frac{\kappa_e}{2}\chi_g. \quad (\text{C15})$$

5. The pumped Kerr modes

To find the resonance frequencies of the susceptibility χ_g , we solve the complex frequency for which $\chi_g^{-1} = 0$. The condition is

$$1 - \left[\mathcal{K}^2 + \frac{\kappa_{\text{nl}}^2}{4} \right] n_c^2 \chi_{\text{pr}} \bar{\chi}_{\text{pr}} = 0, \quad (\text{C16})$$

which is solved by

$$\begin{aligned} \tilde{\omega}_{1,2} &= \omega_p + i\frac{\kappa + 2\kappa_{\text{nl}}n_c}{2} \\ &\pm \sqrt{(\Delta_p - \mathcal{K}n_c)(\Delta_p - 3\mathcal{K}n_c) - \kappa_{\text{nl}}^2 n_c^2 / 4}. \end{aligned} \quad (\text{C17})$$

The real part corresponds to the resonance frequency $\omega_{1,2} = \text{Re}(\tilde{\omega}_{1,2})$ and the imaginary part corresponds to half

the mode linewidth $\kappa_{1,2} = 2 \text{Im}(\tilde{\omega}_{1,2})$. So, in the regime where the argument of the square root is > 0 (always true for our experimental parameters), the system has two resonances

$$\omega_{1,2} = \omega_p \pm \sqrt{(\Delta_p - \mathcal{K}n_c)(\Delta_p - 3\mathcal{K}n_c) - \frac{\kappa_{nl}^2 n_c^2}{4}}, \quad (\text{C18})$$

split symmetrically around the pump frequency. In the experiment and with the parameters we are using, we observe only one of the two modes though, the one at $\omega_2 = \omega'_0$. The shift of this mode with respect to its unpumped frequency ω_0 is given by

$$\delta\omega_0 = \Delta_p - \sqrt{(\Delta_p - \mathcal{K}n_c)(\Delta_p - 3\mathcal{K}n_c) - \frac{\kappa_{nl}^2 n_c^2}{4}}. \quad (\text{C19})$$

When we measure the pumped resonance, we also extract the pumped linewidth

$$\kappa_p = \kappa_0 + 2\kappa_{nl}n_c, \quad (\text{C20})$$

and so the only free parameter when fitting the resonance frequency shift versus pump photon number (see the next subsection) using Eq. (C19) is the Kerr constant \mathcal{K} . For brevity, we also introduce the short version

$$\kappa_1 = \kappa_{nl}n_c. \quad (\text{C21})$$

6. The intracircuit pump photon number

One might expect that we need to know the value of \mathcal{K} to calculate the intracircuit pump photon number from the pump-induced frequency shift and linewidth broadening. This is not the case though, which allows us to first determine n_c and subsequently fit the frequency shift $\delta\omega_0$ as a function of n_c to extract \mathcal{K} from the data. We start by setting $\mathcal{K}n_c = x$ and then solving the characteristic polynomial equation (C6) for x . We get (assuming that $n_c > 0$)

$$x_{1/2} = \Delta_p \pm \sqrt{\frac{\kappa_e n_{in}}{2 n_c} - \frac{\kappa_{eff}^2}{4}}, \quad (\text{C22})$$

where $n_{in} = S_0^2$ and $\kappa_{eff} = \kappa_0 + \kappa_1$. The solution we are interested in is x_2 . Substituting this into Eq. (C19), the frequency relative to the drive

$$\delta = \sqrt{(\Delta_p - x_2)(\Delta_p - 3x_2) - \frac{\kappa_1^2}{4}} \quad (\text{C23})$$

leads to

$$\delta^2 = \sqrt{\frac{\kappa_e n_{in}}{2 n_c} - \frac{\kappa_{eff}^2}{4}} \left(3\sqrt{\frac{\kappa_e n_{in}}{2 n_c} - \frac{\kappa_{eff}^2}{4}} - 2\Delta_p \right) - \frac{\kappa_1^2}{4}. \quad (\text{C24})$$

We can solve this equation for n_c , finding that

$$n_c = \frac{2P_p}{\hbar\omega_p} \frac{\kappa_e}{\kappa_{eff}^2 + 4\tilde{\Delta}^2} \quad (\text{C25})$$

with the effective detuning

$$\tilde{\Delta}^2 = \frac{2}{9} \left[\Delta_p^2 + \Delta_p \sqrt{\Delta_p^2 + 3\delta_\kappa^2} + \frac{3}{2}\delta_\kappa^2 \right] \quad (\text{C26})$$

and

$$\delta_\kappa^2 = \delta^2 + \frac{\kappa_1^2}{4}. \quad (\text{C27})$$

APPENDIX D: ADDITIONAL DATA

1. Impact of junction cutting in devices 2D and 3D₂

In Fig. 1(f), we present the resonances of device 3D₁ before and after cutting the nanoconstrictions at $T_s = 2.5$ K. From the resonance frequencies before and after cutting, ω_b and ω_0 , respectively, we determine the inductance of a single constriction L_c in the device via

$$L_c = 2L \left(\frac{\omega_b^2}{\omega_0^2} - 1 \right); \quad (\text{D1})$$

see Notes II and III within the Supplemental Material [37]. In Fig. 7 we show the analogous data for the other two devices of this work, circuits 2D and 3D₂.

The resonance frequency of device 2D has shifted by the cutting from $\omega_b = 2\pi \cdot 3.995$ GHz to $\omega_0 = 2\pi \cdot 3.981$ GHz, which corresponds to a constriction inductance $L_c^{2D} \approx 8.4$ pH. The total linewidth has increased from $\kappa_b = 2\pi \cdot 1.5$ MHz to $\kappa_0 = 2\pi \cdot 2.4$ MHz. In device 3D₂ the impact of the shift was much larger: the resonance frequency shifted from $\omega_b = 2\pi \cdot 5.047$ GHz to $\omega_0 = 2\pi \cdot 4.811$ GHz, which corresponds to $L_c^{3D2} \approx 103$ pH. The linewidth increased from $\kappa_b = 2\pi \cdot 2.3$ MHz to $\kappa_0 = 2\pi \cdot 24.2$ MHz. The observation that the increase in the linewidths κ is stronger for a larger constriction inductance is not surprising. As we have shown in Fig. 3, the critical temperature of the constrictions is more suppressed for thinner constrictions, and so at the fixed temperature 2.5 K the thinner constrictions presumably have a higher thermal quasiparticle density and at the same time a higher microwave current density. At this point we cannot exclude that there are also other mechanisms at play such as normal conducting contributions at the surfaces or edges of the constrictions that might increase with neon ion milling time, but the overall trend is understandable quite intuitively from the critical temperature suppression. In Note V within the Supplemental Material [37], we also discuss the dependence of the linewidths on the magnetic flux through the SQUIDS.

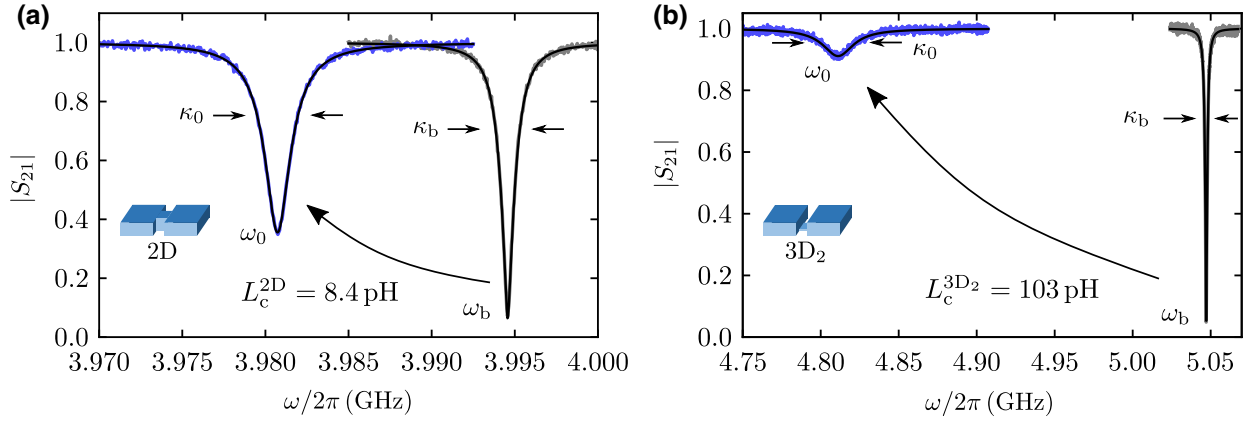


FIG. 7. Impact of constriction cutting in the 2D and 3D₂ circuits. (a) Transmission $|S_{21}|$ versus the probe frequency of circuit 2D before junction cutting (right, gray noisy line) and after junction cutting at the flux sweetspot (left, blue noisy line). (b) Equivalent to (a), but for the 3D₂ circuit. Both panels: noisy lines are data and black smooth lines are fits. Measurement temperature $T_s = 2.5$ K. The resonance frequency and linewidth are ω_b and κ_b before cutting and ω_0 and κ_0 after cutting. From the shift, we determine the additional inductance in the circuit $L_c/2$ (two constrictions in parallel). Values for $\omega_b, \kappa_b, \omega_0, \kappa_0$ can be found in the text.

2. Flux-tuning curves versus the sample temperature in devices 2D and 3D₂

In Fig. 3(a) we show flux-tuning curves of the resonance frequency $\omega_0(\Phi_{\text{ext}})$ for varying sample temperature T_s in circuit 3D₁ and derive from those the critical currents $I_0(T_s)$ and the screening parameters $\beta_L(T_s)$. Since we also show $I_0(T_s)$ and $\beta_L(T_s)$ for the 2D and 3D₂ devices, we present in Figs. 8(a) and 8(b) the corresponding flux-tuning curves for completeness. For both devices, the sweetspot frequency at $\Phi_{\text{ext}} = 0$ decreases with increasing T_s due to the increasing constriction inductance. At the same time the flux-tuning arches get narrower due to a decreasing screening parameter β_L and an increasing inductance participation ratio L_c/L , and the flux-tuning range $\omega_0^{\text{max}} - \omega_0^{\text{min}}$ increases for the same reasons. At the highest temperatures, circuit 2D has a tuning range of about 13 MHz and circuit 3D₂ of about 150 MHz. From the fits to the data, we extract the screening parameter β_L and the linear constriction contribution L_{lin} and calculate the critical current I_0 . The screening parameter β_L and the critical current I_0 are shown in Figs. 3(b) and 3(c); the linear inductance contributions L_{lin} for all three circuits are shown and discussed in Note V within the Supplemental Material [37].

Since the linear inductances in the circuit have a kinetic contribution, the temperature-dependent resonance frequency at the flux sweetspot can be written as

$$\omega_0(T_s) = \frac{1}{\sqrt{C_{\text{tot}}[(L(T_s) + L_{J0}(T_s) + L_{\text{lin}}(T_s))]}}, \quad (\text{D2})$$

where $L_{J0} = \Phi_0[2\pi I_0(T_s)]^{-1}$. In Fig. 8(c), we show the resonance frequency at the sweetspot of all three devices.

APPENDIX E: CALCULATION OF THE KERR NONLINEARITY

For the calculation of the Kerr nonlinearity \mathcal{K} , we follow the method described in Ref. [56] and start with the effective one-dimensional potential for the SQUID, in which each SQUID arm is considered individually (see also Ref. [28]):

$$U = \frac{1}{2}E_{\text{arm}}(\varphi_{\text{left}} - \varphi_1)^2 + \frac{1}{2}E_{\text{arm}}(\varphi_{\text{right}} - \varphi_2)^2 - E_J \cos \varphi_1 - E_J \cos \varphi_2. \quad (\text{E1})$$

Here φ_1, φ_2 are the phase differences of the two Josephson junctions, φ_{left} and φ_{right} are the total phase differences of the left half and the right half of the SQUID loop including the JJs, and the energies are given by

$$E_J = \frac{\Phi_0 I_0}{2\pi}, \quad E_{\text{arm}} = \frac{\Phi_0^2}{4\pi^2 L_{\text{arm}}} \quad (\text{E2})$$

with $L_{\text{arm}} = L_{\text{loop}}/2 + L_{\text{lin}}$. From fluxoid quantization in the SQUID, it follows that

$$\varphi_{\text{right}} - \varphi_{\text{left}} = \varphi_{\text{ext}}, \quad (\text{E3})$$

where $\varphi_{\text{ext}} = 2\pi \Phi_{\text{ext}}/\Phi_0$ is the phase introduced by the external flux. For a visualization of all variables used in this appendix, see Fig. 9.

Then, the potential can be written as a function of a single phase variable $\varphi_s = \varphi_{\text{left}}$ as

$$U[\varphi_s] = \frac{1}{2}E_{\text{arm}}(\varphi_s - \varphi_1[\varphi_s])^2 + \frac{1}{2}E_{\text{arm}}(\varphi_s - \varphi_2[\varphi_s] - \varphi_{\text{ext}})^2 - E_J \cos \varphi_1[\varphi_s] - E_J \cos \varphi_2[\varphi_s], \quad (\text{E4})$$

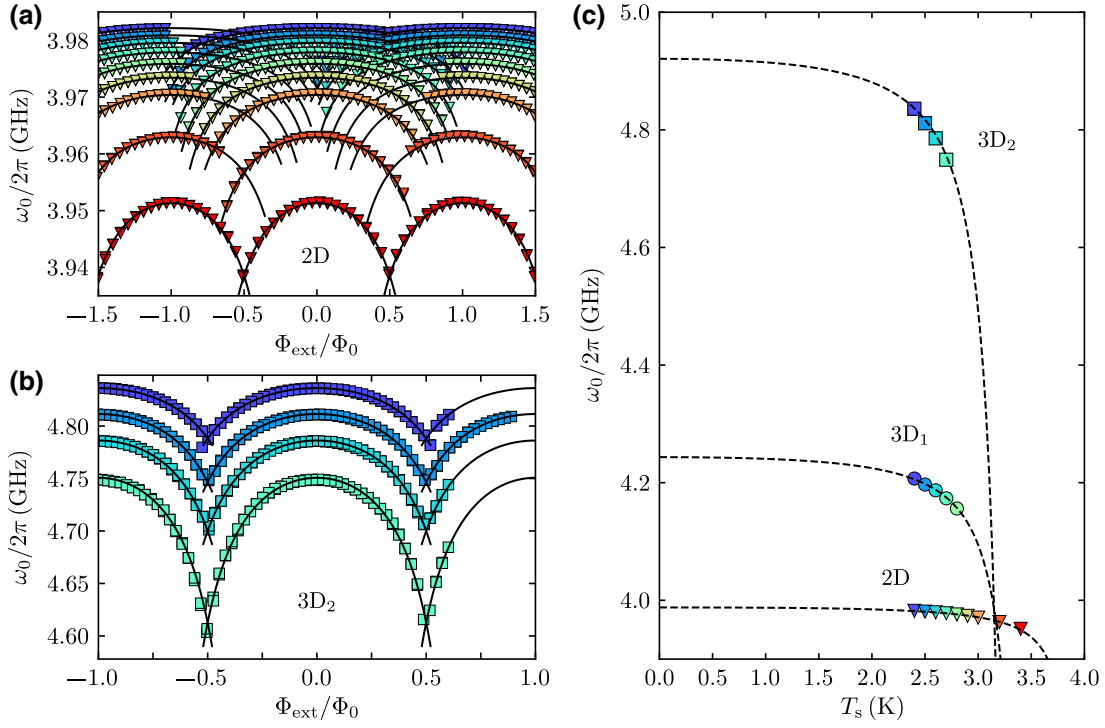


FIG. 8. Temperature dependence of the flux-tuning curves and the sweetspot resonance frequencies. (a) Resonance frequency versus the external bias flux $\omega_0(\Phi_{\text{ext}})$ in device 2D; symbols are data and lines are fits. Data have been taken at temperatures $T_s = (2.4, 2.5, 2.6, 2.7, 2.8, 2.9, 3.0, 3.2, 3.4)$ K (in order from top to bottom). (b) Equivalent of (a), but for device 3D₂. Temperatures are $T_s = (2.4, 2.5, 2.6, 2.7)$ K. Data are partly incomplete due to hysteric jumps (device 2D) and due to insufficient flux data ($\Phi_{\text{ext}}/\Phi_0 > 0.65$ in device 3D₂). (c) Resonance frequency of all three circuits at the sweetspot frequency ($\Phi_{\text{ext}} = 0$) versus the temperature T_s . Symbols are data and the dashed lines are calculated theory lines using Eq. (D2).

and as boundary conditions we have the current conservation relations [56]

$$\varphi_s = \varphi_1 + \zeta \sin \varphi_1, \quad (\text{E5})$$

$$\varphi_s = \varphi_2 + \zeta \sin \varphi_2 - \varphi_{\text{ext}}, \quad (\text{E6})$$

where $\zeta = E_{\text{arm}}/E_J = L_{J0}/L_{\text{arm}}$.

In order to find the Kerr nonlinearity, we have to Taylor expand the potential up to fourth order, i.e.,

$$\begin{aligned} \frac{U(\varphi_s)}{E_J} &= c_0 + c_1(\varphi_s - \varphi_{s,\min}) + \frac{c_2}{2}(\varphi_s - \varphi_{s,\min})^2 \\ &+ \frac{c_3}{6}(\varphi_s - \varphi_{s,\min})^3 + \frac{c_4}{24}(\varphi_s - \varphi_{s,\min})^4, \end{aligned} \quad (\text{E7})$$

where the coefficients are determined by the n th derivative of the potential evaluated at the phase at the potential well minimum $\varphi_{s,\min}$:

$$c_n = \frac{1}{E_J} \left. \frac{\partial^n U}{\partial \varphi_s^n} \right|_{\varphi_{s,\min}}. \quad (\text{E8})$$

To find the value for $\varphi_{s,\min}$, we demand that in the minimum we have $c_1 = 0$ and, as a result, we get

$$\varphi_{s,\min} = \frac{1}{2}(\varphi_{1,\min} + \varphi_{2,\min} - \varphi_{\text{ext}}). \quad (\text{E9})$$

In the potential minimum, however, i.e., without any phase excitation, we also have

$$\sin \varphi_{1,\min} = -\sin \varphi_{2,\min} \implies \varphi_{1,\min} = -\varphi_{2,\min}, \quad (\text{E10})$$

since the same SQUID circulating current $J = -I_0 \sin \varphi_1 = I_0 \sin \varphi_2$ is flowing through both JJs in opposite directions. Then, using Eq. (E9), we can conclude that

$$\varphi_{s,\min} = -\frac{\varphi_{\text{ext}}}{2}, \quad (\text{E11})$$

and using Eq. (E5), we arrive at

$$\varphi_{1,\min} + \zeta \sin \varphi_{1,\min} + \frac{\varphi_{\text{ext}}}{2} = 0, \quad (\text{E12})$$

which is completely equivalent to

$$\frac{\Phi}{\Phi_0} = \frac{\Phi_{\text{ext}}}{\Phi_0} - \frac{\beta_L}{2} \sin \left(\pi \frac{\Phi}{\Phi_0} \right) \quad (\text{E13})$$

with screening parameter β_L , total flux in the SQUID Φ , and using the relation $\varphi_{1,\min} = -\pi(\Phi)/\Phi_0$. For the

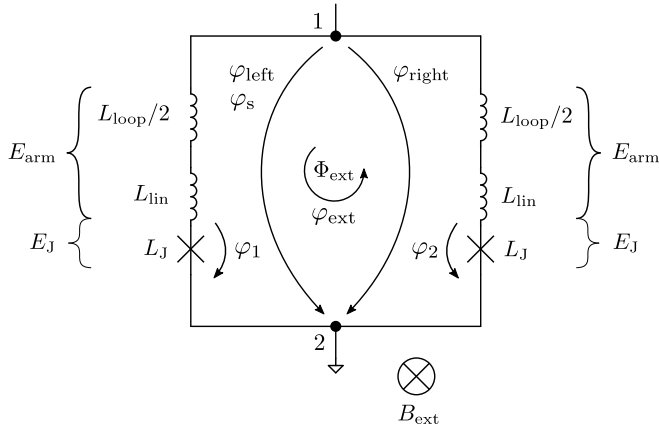


FIG. 9. Schematic SQUID circuit with definitions of all variables used for the calculation of the Kerr constant. Circuit equivalent of the SQUID with a linear loop inductance $L_{\text{loop}}/2$ in each arm and a constriction modeled by a linear inductance L_{lin} and a sinusoidal Josephson contribution L_J . In each arm the energy $E_J + E_{\text{arm}}$ is stored, where E_J is the Josephson energy and E_{arm} is the energy stored in the linear contribution. Nodes 1 and 2 subdivide the loop into a left half and right half with total phase differences φ_{left} and φ_{right} between the nodes. The single phase variable φ_s is identical to φ_{left} . The Josephson contributions of the arms have phase differences φ_1 and φ_2 , respectively. By applying an external magnetic field B_{ext} perpendicular to the SQUID loop, an external phase φ_{ext} is introduced by the external flux Φ_{ext} .

derivatives, we get

$$\frac{\partial U}{\partial \varphi_s} = E_{\text{arm}}(2\varphi_s - \varphi_1[\varphi_s] - \varphi_2[\varphi_s] + \varphi_{\text{ext}}), \quad (\text{E14})$$

$$\frac{\partial^2 U}{\partial \varphi_s^2} = E_{\text{arm}} \left(2 - \frac{\partial \varphi_1}{\partial \varphi_s} - \frac{\partial \varphi_2}{\partial \varphi_s} \right), \quad (\text{E15})$$

$$\frac{\partial^3 U}{\partial \varphi_s^3} = -E_{\text{arm}} \left(\frac{\partial^2 \varphi_1}{\partial \varphi_s^2} + \frac{\partial^2 \varphi_2}{\partial \varphi_s^2} \right), \quad (\text{E16})$$

$$\frac{\partial^4 U}{\partial \varphi_s^4} = -E_{\text{arm}} \left(\frac{\partial^3 \varphi_1}{\partial \varphi_s^3} + \frac{\partial^3 \varphi_2}{\partial \varphi_s^3} \right), \quad (\text{E17})$$

and we can obtain the phase derivatives from Eqs. (E5) and (E6) as

$$\frac{\partial \varphi_s}{\partial \varphi_1} = 1 + \zeta \cos \varphi_1, \quad (\text{E18})$$

$$\frac{\partial \varphi_s}{\partial \varphi_2} = 1 + \zeta \cos \varphi_2, \quad (\text{E19})$$

which can be inverted as

$$\frac{\partial \varphi_1}{\partial \varphi_s} = \frac{1}{1 + \zeta \cos \varphi_1}, \quad (\text{E20})$$

$$\frac{\partial \varphi_2}{\partial \varphi_s} = \frac{1}{1 + \zeta \cos \varphi_2}. \quad (\text{E21})$$

The consecutive derivatives are, for $j = 1, 2$,

$$\frac{\partial^2 \varphi_j}{\partial \varphi_s^2} = \frac{\zeta \sin \varphi_j}{(1 + \zeta \cos \varphi_j)^3}, \quad (\text{E22})$$

$$\frac{\partial^3 \varphi_j}{\partial \varphi_s^3} = \frac{\zeta \cos \varphi_j (1 + \zeta \cos \varphi_j) + 3\zeta^2 \sin^2 \varphi_j}{(1 + \zeta \cos \varphi_j)^5}, \quad (\text{E23})$$

which we can finally use to express our Taylor coefficients with $\varphi_0 = -\varphi_{1,\text{min}} = \pi(\Phi)/\Phi_0$ as

$$c_2 = \frac{2 \cos \varphi_0}{1 + \zeta \cos \varphi_0}, \quad (\text{E24})$$

$$c_3 = 0, \quad (\text{E25})$$

$$c_4 = -2 \frac{\cos \varphi_0 (1 + \zeta \cos \varphi_0) + 3\zeta \sin^2 \varphi_0}{(1 + \zeta \cos \varphi_0)^5}. \quad (\text{E26})$$

The SQUID inductance and Kerr nonlinearity of the SQUID, when shunted with C_{tot} , are now given by [56]

$$L_s = \frac{L_{J0}}{c_2} = \frac{1}{2}(L_J + L_{\text{arm}}) \quad (\text{E27})$$

and

$$\begin{aligned} \mathcal{K}_s &= \frac{e^2}{2\hbar C_{\text{tot}}} \frac{c_4}{c_2} \\ &= -\frac{e^2}{2\hbar C_{\text{tot}}} \left(\frac{L_J}{L_{\text{arm}} + L_J} \right)^3 \left[1 + 3 \frac{L_{\text{arm}}}{L_{\text{arm}} + L_J} \tan^2 \varphi_0 \right], \end{aligned} \quad (\text{E28})$$

where $L_J = L_{J0}/\cos \varphi_0$, e is the elementary charge, and \hbar is the reduced Planck number.

When we add a linear inductance $L - L_{\text{loop}}/4$ in series, we get the modified parameters [56]

$$\tilde{c}_2 = p c_2, \quad (\text{E29})$$

$$L_{\text{tot}} = \frac{L_s}{p}, \quad (\text{E30})$$

$$\tilde{c}_4 = p^4 c_4, \quad (\text{E31})$$

$$\mathcal{K} = p^3 \mathcal{K}_s, \quad (\text{E32})$$

where p is the inductance participation ratio

$$p = \frac{L_s}{L - L_{\text{loop}}/4 + L_s}. \quad (\text{E33})$$

Then, we finally have the explicit expression for the circuit Kerr nonlinearity

$$\mathcal{K} = -\frac{e^2}{2\hbar C_{\text{tot}}} \left(\frac{L_J}{2L + L_{\text{lin}} + L_J} \right)^3 \left[1 + 3 \frac{L_{\text{arm}}}{L_{\text{arm}} + L_J} \tan^2 \varphi_0 \right]. \quad (\text{E34})$$

- [1] J. Clarke and F. K. Wilhelm, Superconducting quantum bits, *Nature* **453**, 1031 (2008).
- [2] J. Q. You and Franco Nori, Atomic physics and quantum optics using superconducting circuits, *Nature* **474**, 589 (2011).
- [3] A. Blais, A. L. Grimsmo, S. M. Girvin, and A. Wallraff, Circuit quantum electrodynamics, *Rev. Mod. Phys.* **93**, 025005 (2021).
- [4] F. Arute *et al.*, Quantum supremacy using a programmable superconducting processor, *Nature* **574**, 505 (2019).
- [5] M. A. Castellanos-Beltran, K. D. Irwin, G. C. Hilton, L. R. Vale, and K. W. Lehnert, Amplification and squeezing of quantum noise with a tunable Josephson metamaterial, *Nat. Phys.* **4**, 929 (2008).
- [6] N. Bergeal, F. Schackert, M. Metcalfe, R. Vijay, V. E. Manucharyan, L. Frunzio, D. E. Prober, R. J. Schoelkopf, S. M. Girvin, and M. H. Devoret, Phase-preserving amplification near the quantum limit with a Josephson ring modulator, *Nature* **465**, 64 (2010).
- [7] C. Macklin, K. O'Brien, D. Hover, M. E. Schwartz, V. Bolkhovskiy, X. Zhang, W. D. Oliver, and I. Siddiqi, A near-quantum-limited Josephson traveling-wave parametric amplifier, *Science* **350**, 307 (2015).
- [8] M. Hatridge, R. Vijay, D. H. Slichter, J. Clarke, and I. Siddiqi, Dispersive magnetometry with a quantum limited SQUID parametric amplifier, *Phys. Rev. B* **83**, 134501 (2011).
- [9] E. M. Levenson-Falk, N. Antler, and I. Siddiqi, Dispersive nanoSQUID magnetometry, *Supercond. Sci. Technol.* **29**, 113003 (2016).
- [10] J. R. Johansson, G. Johansson, and F. Nori, Optomechanical-like coupling between superconducting resonators, *Phys. Rev. A* **90**, 053833 (2014).
- [11] C. Eichler and J. R. Petta, Realizing a circuit analog of an optomechanical system with longitudinally coupled superconducting resonators, *Phys. Rev. Lett.* **120**, 227702 (2018).
- [12] D. Bothner, I. C. Rodrigues, and G. A. Steele, Photon-pressure strong coupling between two superconducting circuits, *Nat. Phys.* **17**, 85 (2021).
- [13] I. C. Rodrigues, G. A. Steele, and D. Bothner, Parametrically enhanced interactions and nonreciprocal bath dynamics in a photon-pressure Kerr amplifier, *Sci. Adv.* **8**, eabq1690 (2022).
- [14] O. Shevchuk, G. A. Steele, and Ya. M. Blanter, Strong and tunable couplings in flux-mediated optomechanics, *Phys. Rev. B* **96**, 014508 (2017).
- [15] I. C. Rodrigues, D. Bothner, and G. A. Steele, Coupling microwave photons to a mechanical resonator using quantum interference, *Nat. Commun.* **10**, 5359 (2019).
- [16] P. Schmidt, M. T. Amawi, S. Pogorzalek, F. Deppe, A. Marx, R. Gross, and H. Huebl, Sideband-resolved resonator electromechanics based on a nonlinear Josephson inductance probed on the single-photon level, *Commun. Phys.* **3**, 233 (2020).
- [17] D. Zoepfl, M. L. Juan, N. Diaz-Naufal, C. M. F. Schneider, L. F. Deeg, A. Sharafiev, A. Metelmann, and G. Kirchmair, Kerr enhanced backaction cooling in magnetomechanics, *Phys. Rev. Lett.* **130**, 033601 (2023).
- [18] Y. Nakamura, Yu. A. Pashkin, and J. S. Tsai, Coherent control of macroscopic quantum states in a single-Cooper-pair box, *Nature* **398**, 786 (1999).
- [19] A. Palacios-Laloy, F. Nguyen, F. Mallet, P. Bertet, D. Vion, and D. Esteve, Tunable resonators for quantum circuits, *J. Low Temp. Phys.* **151**, 1034 (2008).
- [20] R. Meservey and P. M. Tedrow, Properties of very thin aluminum films, *J. Appl. Phys.* **42**, 51 (1971).
- [21] K. Borisov, D. Rieger, P. Winkel, F. Henriques, F. Valenti, A. Ionita, M. Wessbecher, M. Spiecker, D. Gusenkova, I. M. Pop, and W. Wernsdorfer, Superconducting granular aluminum resonators resilient to magnetic fields up to 1 Tesla, *Appl. Phys. Lett.* **117**, 120502 (2020).
- [22] J. Krause, C. Dickel, E. Vaal, M. Vielmetter, J. Feng, R. Bounds, G. Catelani, J. M. Fink, and Y. Ando, Magnetic field resilience of three-dimensional transmons with thin-film Al/AlO_x/Al Josephson junctions approaching 1 T, *Phys. Rev. Appl.* **17**, 034032 (2022).
- [23] S. E. de Graaf, A. V. Danilov, A. Adamyan, T. Bauch, and S. E. Kubatkin, Magnetic field resilient superconducting fractal resonators for coupling to free spins, *J. Appl. Phys.* **112**, 123905 (2012).
- [24] N. Samkharadze, A. Bruno, P. Scarlino, G. Zheng, D. P. DiVincenzo, L. DiCarlo, and L. M. K. Vandersypen, High-kinetic-inductance superconducting nanowire resonators for circuit QED in a magnetic field, *Phys. Rev. Appl.* **5**, 044004 (2016).
- [25] C. W. Zollitsch, J. O'Sullivan, O. Kennedy, G. Dold, and J. J. L. Morton, Tuning high-Q superconducting resonators by magnetic field reorientation, *AIP Adv.* **9**, 125225 (2019).
- [26] A. Ghirri, C. Bonizzoni, D. Gerace, S. Sanna, A. Cassinese, and M. Affronte, YBa₂Cu₃O₇ microwave resonators for strong collective coupling with spin ensembles, *Appl. Phys. Lett.* **106**, 184101 (2015).
- [27] A. Roitman, A. Shaulov, and Y. Yeshurun, Characterization of YBa₂Cu₃O_{7- δ} coplanar resonator for microwave kinetic inductance detectors, *Supercond. Sci. Technol.* **36**, 015002 (2023).
- [28] K. Uhl, D. Hackenbeck, C. Fuger, R. Kleiner, D. Koelle, and D. Bothner, A flux-tunable YBa₂Cu₃O₇ quantum interference microwave circuit, *Appl. Phys. Lett.* **122**, 182603 (2023).
- [29] E. J. Romans, S. Rozhko, L. Young, A. Blois, L. Hao, D. Cox, and J. C. Gallop, Noise performance of niobium nano-SQUIDS in applied magnetic fields, *IEEE Trans. Appl. Supercond.* **21**, 404 (2011).
- [30] O. W. Kennedy, J. Burnett, J. C. Fenton, N. G. N. Constantino, P. A. Warburton, J. J. L. Morton, and E. Dupont-Ferrier, Tunable Nb superconducting resonator based on a constriction nano-SQUID fabricated with a Ne focused ion beam, *Phys. Rev. Appl.* **11**, 014006 (2019).
- [31] M. Xu, R. Cheng, Y. Wu, G. Liu, and H. X. Tang, Magnetic field-resilient quantum-limited parametric amplifier, *PRX Quantum* **4**, 010322 (2023).
- [32] V. Bouchiat, M. Faucher, C. Thirion, W. Wernsdorfer, T. Fourmier, and B. Pannetier, Josephson junctions and superconducting quantum interference devices made by local oxidation of niobium ultrathin films, *Appl. Phys. Lett.* **79**, 123 (2001).

- [33] K. Hasselbach, D. Mailly, and J. R. Kirtley, Microsuperconducting quantum interference device characteristics, *J. Appl. Phys.* **91**, 4432 (2002).
- [34] E. E. Mitchell and S. K. H. Lam, Niobium dc SQUIDs with nanobridge junctions, *Phys. Procedia* **36**, 382 (2012).
- [35] H. Wang, L. Chen, X. Liu, L. Wu, X. Wu, L. You, and Z. Wang, Fabrication and characterization of miniaturized NbN superconducting quantum interference devices with nanobridge junctions, *IEEE Trans. Appl. Supercond.* **27**, 1601905 (2017).
- [36] S. Pogorzalek, K. G. Fedorov, L. Zhong, J. Goetz, F. Wulschner, M. Fischer, P. Eder, E. Xie, K. Inomata, T. Yamamoto, Y. Nakamura, A. Marx, F. Deppe, and R. Gross, Hysteretic flux response and nondegenerate gain of flux-driven Josephson parametric amplifiers, *Phys. Rev. Appl.* **8**, 024012 (2017).
- [37] See Supplemental Material at <http://link.aps.org/supplemental/10.1103/PhysRevApplied.21.024051> for further details about the power calibration, the theoretical device description, the fitting routine, the error bar calculation, and additional data, which also includes Refs. [61,62].
- [38] R. Vijay, E. M. Levenson-Falk, D. H. Slichter, and I. Siddiqi, Approaching ideal weak link behavior with three dimensional aluminum nanobridges, *Appl. Phys. Lett.* **96**, 223112 (2010).
- [39] L. Chen, H. Wang, X. Liu, L. Wu, and Z. Wang, A high-performance Nb nano-superconducting quantum interference device with a three-dimensional structure, *Nano Lett.* **16**, 7726 (2016).
- [40] M. M. Khapaev, A. Yu. Kidiyarova-Shevchenko, P. Magneind, and M. Yu. Kupriyanov, 3D-MLSI: Software package for inductance calculation in multilayer superconducting integrated circuits, *IEEE Trans. Appl. Supercond.* **11**, 1090 (2001).
- [41] J. Wenner, M. Neeley, Radoslav C. Bialczak, M. Lenander, E. Lucero, A. D. O'Connell, D. Sank, H. Wang, M. Weides, A. N. Cleland, and J. M. Martinis, Wirebond crosstalk and cavity modes in large chip mounts for superconducting qubits, *Supercond. Sci. Technol.* **24**, 065001 (2011).
- [42] D. Rieger, S. Günzler, M. Spiecker, A. Nambisan, W. Wernsdorfer, and I. M. Pop, Fano interference in microwave resonator measurements, *Phys. Rev. Appl.* **20**, 014059 (2023).
- [43] D. Hazra, J. R. Kirtley, and K. Hasselbach, Retrapping current in bridge-type nano-SQUIDs, *Phys. Rev. Appl.* **4**, 024021 (2015).
- [44] G. De Simoni, C. Puglia, and F. Giazotto, Niobium Dayem nano-bridge Josephson gate-controlled transistors, *Appl. Phys. Lett.* **116**, 242601 (2020).
- [45] Z. Qing, T. Yuchien, L. Jinjin, L. Hao, J. Kaili, Z. Yuan, C. Wenhui, M. Zhang, and W. Xueshen, High transfer coefficient niobium nano-SQUID integrated with a nanogap modulation flux line, *Meas. Sci. Technol.* **32**, 025001 (2021).
- [46] M. Wyss, K. Bagani, D. Jetter, E. Marchiori, A. Vervelaki, B. Gross, J. Ridderbos, S. Gliga, C. Schönenberger, and M. Poggio, Magnetic, thermal, and topographic imaging with a nanometer-scale SQUID-on-lever scanning probe, *Phys. Rev. Appl.* **17**, 034002 (2022).
- [47] E. M. Levenson-Falk, F. Kos, R. Vijay, L. Glazman, and I. Siddiqi, Single-quasiparticle trapping in aluminum nanobridge Josephson junctions, *Phys. Rev. Lett.* **112**, 047002 (2014).
- [48] I. Nsanzeza and B. L. T. Plourde, Trapping a single vortex and reducing quasiparticles in a superconducting resonator, *Phys. Rev. Lett.* **113**, 117002 (2014).
- [49] K. K. Likharev, Superconducting weak links, *Rev. Mod. Phys.* **51**, 101 (1979).
- [50] A. Gumann, T. Dahm, and N. Schopohl, Microscopic theory of superconductor-constriction-superconductor Josephson junctions in a magnetic field, *Phys. Rev. B* **76**, 064529 (2007).
- [51] A. G. P. Troeman, S. H. W. van der Ploeg, E. Il'ichev, H.-G. Meyer, A. A. Golubov, M. Yu. Kupriyanov, and H. Hilgenkamp, Temperature dependence measurements of the supercurrent-phase relationship in niobium nanobridges, *Phys. Rev. B* **77**, 024509 (2008).
- [52] D. Bothner, I. C. Rodrigues, and G. A. Steele, Four-wave-cooling to the single phonon level in Kerr optomechanics, *Commun. Phys.* **5**, 33 (2022).
- [53] I. C. Rodrigues, D. Bothner, and G. A. Steele, Cooling photon-pressure circuits into the quantum regime, *Sci. Adv.* **7**, eabg6653 (2021).
- [54] E. M. Levenson-Falk, R. Vijay, and I. Siddiqi, Nonlinear microwave response of aluminum weak-link Josephson oscillators, *Appl. Phys. Lett.* **98**, 123115 (2011).
- [55] J. Bardeen, Critical fields and currents in superconductors, *Rev. Mod. Phys.* **34**, 667 (1962).
- [56] N. E. Frattini, V. V. Sivak, A. Lingenfelter, S. Shankar, and M. H. Devoret, Optimizing the nonlinearity and dissipation of a SNAIL parametric amplifier for dynamic range, *Phys. Rev. Appl.* **10**, 054020 (2018).
- [57] D. Zoepfl, M. L. Juan, C. M. F. Schneider, and G. Kirchmair, Single-photon cooling in microwave magnetomechanics, *Phys. Rev. Lett.* **125**, 023601 (2020).
- [58] F. Fani Sani, I. C. Rodrigues, D. Bothner, and G. A. Steele, Level attraction and idler resonance in a strongly driven Josephson cavity, *Phys. Rev. Res.* **3**, 043111 (2021).
- [59] www.zenodo.org/records/10618057.
- [60] M. F. Gely, A. Sanz Mora, S. Yanai, R. van der Spek, D. Bothner, and G. A. Steele, Apparent nonlinear damping triggered by quantum fluctuations, *Nat. Commun.* **14**, 7566 (2023).
- [61] N. Klein, H. Chaloupka, G. Müller, S. Orbach, and H. Piel, The effective microwave surface impedance of high- T_c thin films, *J. Appl. Phys.* **67**, 6940 (1990).
- [62] R. Igreja and C. J. Dias, Analytical evaluation of the interdigital electrodes capacitance for a multi-layered structure, *Sens. Actuators A* **112**, 291 (2004).